

Polarization observables in the ${}^1\text{H}(\vec{e}, e'K^+)\vec{\Lambda}^0$
reaction.

Spokesmen: Daniel S. Carman^a, Kyungseon Joo^h,
Laird Kramer^e, Brian A. Raue^e

Participants: S. P. Barrow^f, C. Bennhold^b, W. Boeglin^e,
M. Coman^e, L. Dennis^f, F. Klein^d, S. Kuhn^g,
P. Markowitz^e, T. Mart^c, M. D. Mestayer^d, C. Meyer^a,
R. Minehart^h, R. Nasseripour^e, B. Quinn^a, J. Reinhold^e,
R. Schumacher^a

^aCarnegie Mellon University, Pittsburgh, PA 15213

^bGeorge Washington University, Washington, DC 20052

^cUniversitas Indonesia, Depok 16424, Indonesia

^dJefferson Lab, Newport News, VA 23606

^eFlorida International University, Miami, FL 33199

^fFlorida State University, Tallahassee, FL 32306

^gOld Dominion University, Norfolk, VA 23529

^hUniversity of Virginia, Charlottesville, VA 22901

December 16, 1998

1 Abstract

This proposal describes an experiment to measure polarization observables in the $\bar{e}p \rightarrow e'K^+\bar{\Lambda}$ reaction at 2.4 and 4.0 GeV using the CLAS spectrometer in Hall B. The large acceptance of CLAS will enable us to detect the scattered electron, the kaon, and the Λ -hyperon decay proton over a range of Q^2 from 0.4 to 2.7 (GeV/c)² and W from 1.6 to 2.4 GeV. The measured angular correlation of the decay proton will allow for the determination of the Λ polarization. The large acceptance of CLAS enables simultaneous study of the reaction over varying kinematical regions where the different s , t , or u channel processes have varying strengths. By emphasizing specific channel processes we can effectively limit the intermediate baryonic or mesonic resonances involved in the reaction.

Our experiment proposes to provide the first ever double-polarization measurements for this elementary electroproduction process. The electroproduction reaction provides insight into the basic reaction mechanism (resonance formation and decay, polarization, and interference effects), and information regarding fundamental hadronic structure information (electromagnetic form factors). Our experiment proposes to measure the six electron-beam helicity-dependent and helicity-independent Λ polarization components. A subset of these have factors that include the response functions $R_{TT'}$ and $R_{TL'}$, which are in turn sensitive to the Λ magnetic form factor and the $K^+K^{*\gamma}$ transition form factor. Using the CLAS provides a unique opportunity to probe these response functions well beyond the usual parallel or in-plane kinematics by studying them over a broad range of t and kaon azimuthal angle. This experiment represents a stepping stone to improved kaon electroproduction observables.

In hadrodynamical models, the polarization observables are sensitive to the details of the reaction mechanism; that is, the number of intermediate resonances involved in the reaction, as well as their coupling constants. From the point of view of quark models, the double-polarization observables will shed light on descriptions of strong decays through $q\bar{q}$ pair production and address the ambiguity in the quantum numbers of the created $s\bar{s}$ pair created in the intermediate state. As well, our kinematics span a transition regime where it is expected that the hadrodynamical formalism will begin to give way to a description in terms of quarks and gluons. Newly developed gauge invariant models based on Regge exchanges may provide a convenient formalism over these kinematics as well as above the resonance region.

Contents

1	Abstract	ii
2	Introduction	1
2.1	Formalism	4
2.2	Hadrodynamic Models	8
2.3	Quark Models	11
2.4	Regge Theory	16
3	Experimental Overview	19
3.1	CLAS Acceptance Studies	20
3.1.1	Electron Kinematics and Acceptance Limits	20
3.1.2	Kaon Kinematics and Acceptance Limits	22
3.1.3	Proton Kinematics and Acceptance Limits	23
3.2	Particle Identification and Backgrounds	26
3.3	Data Binning and Statistical Precision	26
4	Monte Carlo Study	33
4.1	Generation of $\vec{e}p \rightarrow e'K^+\vec{\Lambda}$	33
4.2	Generation of $\Lambda \rightarrow p + \pi^-$	35
4.3	Measurement of Induced Polarization of Λ	36
4.4	Simulation of the Transferred/Induced Λ Polarization	39
5	Systematic Uncertainties	45
6	Summary	47
7	Beam-time Request	49
8	Appendix	50
8.1	Kinematics	50
8.2	Response functions	51

2 Introduction

We propose to use the CEBAF Large Acceptance Spectrometer to measure the polarization of lambdas produced by polarized electrons on an unpolarized hydrogen target at 2.4 and 4.0 GeV. This measurement will place constraints on the kaon and lambda magnetic form factors and will test hadrodynamic and quark descriptions of the electromagnetic production of kaons. The present state of understanding of the kaon photo- and electroproduction processes is limited by a sparsity of data. Existing cross section measurements cover a limited range of kinematics and suffer from relatively large experimental uncertainties (reviewed in ref. [1]). This leads to large uncertainties in constraining existing models such as hadronic-field theories [1, 2, 3] or quark-based models [4, 5]. While much remains to be done, recent Jefferson Lab experiments have already made significant headway in improving the data base. Experiments in Hall C [6, 7] have measured electroproduction cross sections on hydrogen and deuterium targets and recently presented the first high precision longitudinal and transverse structure function (σ_L and σ_T) data [8].

Further information on the electromagnetic production of kaons will come from the other Halls. In Halls A and B [9, 10] experiments will extend the kinematic range of the σ_L and σ_T measurements as well as provide measurements of the interference terms σ_{TT} and σ_{LT} . Kaon photoproduction [11] and electroproduction [12] experiments will be done in Hall B in which the polarization of the outgoing hyperon (either a Λ^0 or a Σ^0) is measured. The hyperon's polarization provides yet another constraint on models. Our proposed measurement uses the newly available high-polarization electron beam and measures the lambda polarization to determine double-polarization observables. These data will access previously unmeasured response functions (for a full listing of the 36 response functions see Table 7 in the appendix) which are inaccessible through any other process and will further add to our understanding of strangeness production. A similar experiment in Hall C has been approved [13] but covers a limited region of kinematics compared to this proposed experiment.

The $\vec{e}p \rightarrow e'K^+\vec{\Lambda}^0$ reaction provides the opportunity to study physics not accessible in other reactions. The simple fact that there are no valence s quarks in the proton means that we are studying strangeness production mechanisms which are absent in, for example, pion-production experiments. We can study s -channel processes that specifically *exclude* the Δ since the $K^+\Lambda^0$ final state has isospin 1/2. Using a polarized electron beam and utilizing the self-analyzing nature of the Λ allows us to look at various spin characteristics of the reaction. In particular, this reaction may shed light on the quantum numbers of the $s\bar{s}$ pair

created in the intermediate state.

Our measurement of double-polarization observables with the electroproduction process is complementary to the photoproduction measurements (a limited study of the latter was done for the first time during the g1 run period of CLAS). Because the virtual photon has longitudinal as well as transverse polarization, electroproduction allows access to longitudinal and longitudinal/transverse interference response functions. Electroproduction also enables a study of the Q^2 dependence of $K\Lambda$ production. Furthermore, it might be expected that the VMD diagram will be suppressed in electroproduction relative to photoproduction as the virtual ϕ meson is produced further off shell with virtual photons. Thus the propagator, and hence the production probability, is reduced.

Studying the elementary strangeness production process with electromagnetic probes offers an advantage over similar studies with hadronic probes. In this reaction the distortions in the incident and outgoing channels are largely reduced due to the rather weakly interacting nature of both the electron and the scattered K^+ with hadrons. The reduction in cross section of this weak process relative to the strong reaction processes is not an issue at CEBAF as the luminosities achievable more than compensate for the difference. Furthermore, electroproduction will provide information that is complementary to that from hadronic reactions such as (K, π) and $(p, p'K)$.

Using the CLAS to study this reaction leads to a number of advantages over similar studies using other facilities. The large three-body acceptance of CLAS will allow us to detect the scattered electron, the kaon, and the proton from the decay of the Λ hyperon. The large angular acceptance for the decay proton enables good determination of the Λ polarization. Furthermore, the large acceptance of CLAS also allows us to concurrently study the reaction over varying kinematical regions where the relative importance of the s , t , and u channels will vary. By emphasizing specific channel processes we can limit the intermediate baryonic or mesonic resonances involved in the reaction.

In hadrodynamical models, information from double-polarization observables is critical to achieve sensitivity to response functions not accessible to no-polarization or single-polarization experiments. The response functions are functions of complex reaction amplitudes (see, for example, Ref. [1]). s , t , and u channels all contribute to the electroproduction (or photoproduction) process in varying degrees depending on kinematics and each may go through any number of intermediate hadronic resonances (see Fig. 1). The presence of all these possible production mechanisms means that reliable hadrodynamical models require many parameters and thus many observables to constrain the parameters [1, 2, 3]. Double-polarization observables place constraints on these parameters while also

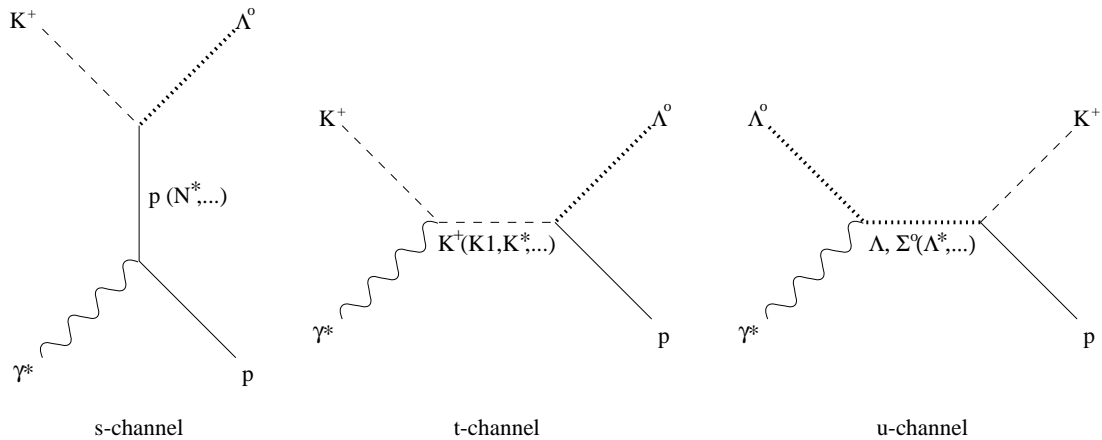


Figure 1: Resonance-picture Feynman diagrams for the process $\gamma^* p \rightarrow K^+ \Lambda$ for s -, t -, and u -channel reactions. The non-Born terms are within the parentheses.

providing for more stringent tests of existing models.

Double-polarization measurements using the $\vec{e}p \rightarrow e'K^+\vec{\Lambda}$ reaction should also lead to a better understanding of strangeness production within a quark picture. Fig. 2 shows three possible production processes. Naively, since the spin of the Λ is carried by the s -quark [14], the polarization of the outgoing Λ is directly related to the relative spin alignment of the produced strange-quark pair and the target proton's constituent uud quarks. A more sophisticated quark picture must include intermediate resonances. Therefore, extracting any information about the spins of the proton quarks or the created quark pair can only be done within the framework of a model. The decay of non-strange baryons (produced in the s channel) into the ΛK final state has been recently examined in a relativized quark-pair creation model [4]. With the addition of the polarization observables measured in this experiment, decay widths can be extracted—either by direct identification of narrowly binned states or in a partial wave analysis—for comparison to the model. By testing the model an understanding of the spin alignment of the quarks can be inferred.

Finally, another promising avenue for the description of the elementary photo- and electroproduction of strangeness is a Regge description [5, 15]. This model is valid above the resonance region ($E_\gamma \geq 4$ GeV) at intermediate momentum transfers ($-t \leq 3$ (GeV/c)²). The gauge invariant reaction mechanism is modeled through t channel K and K^* exchanges. This model has proven to be superior

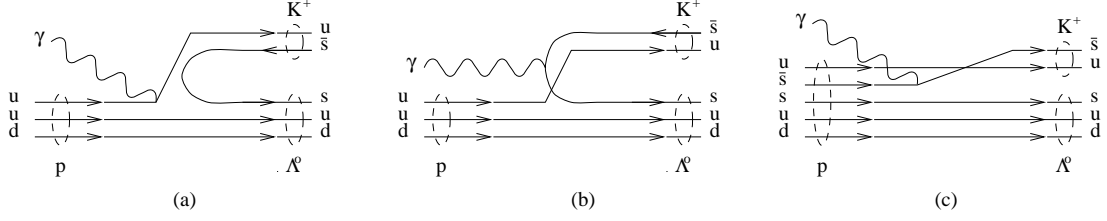


Figure 2: Some of the possible quark diagrams for $K\Lambda$ production. (a) s -channel Born diagram, (b) VMD diagram, (c) direct knockout of anti-strange quark.

to Born-diagram models for describing the sparse cross section and asymmetry data. Experimental data, particularly polarization observables, are necessary for the further development of this type of model.

2.1 Formalism

The most general form of the cross section for kaon electroproduction with a polarized beam and a polarized target is given by:

$$\frac{d^5\sigma}{d\Omega_{E'}d\Omega_KdE'} = \Gamma \frac{d\sigma_\nu}{d\Omega_K}. \quad (1)$$

The kinematic factors are defined in Appendix 8.1. The virtual photon cross section is given in terms of the response functions $R_i^{\beta\alpha}$ [16] as:

$$\begin{aligned} \frac{d\sigma_\nu}{d\Omega_K} = & K S_\alpha S_\beta \left[R_T^{\beta\alpha} + \epsilon_L R_L^{\beta\alpha} + \sqrt{2\epsilon_L(1+\epsilon)} ({}^c R_{TL}^{\beta\alpha} \cos \phi_K + {}^s R_{TL}^{\beta\alpha} \sin \phi_K) \right. \\ & + \epsilon ({}^c R_{TT}^{\beta\alpha} \cos 2\phi_K + {}^s R_{TT}^{\beta\alpha} \sin 2\phi_K) \\ & \left. + h\sqrt{2\epsilon_L(1-\epsilon)} ({}^c R_{TL'}^{\beta\alpha} \cos \phi_K + {}^s R_{TL'}^{\beta\alpha} \sin \phi_K) + h\sqrt{1-\epsilon^2} R_{TT'}^{\beta\alpha} \right]. \quad (2) \end{aligned}$$

ϕ_K is the angle of the K - Λ hadron plane with respect to the electron scattering plane. The momenta and angles are shown in Fig. 3. h is the electron-beam helicity. The superscripts α and β refer to the target and Λ polarizations respectively, where a sum over α and β is implied. The left superscripts on the response functions, c and s , refer to the cosine or sine term, respectively. Table 7 in the appendix shows which response functions survive for various polarization conditions.

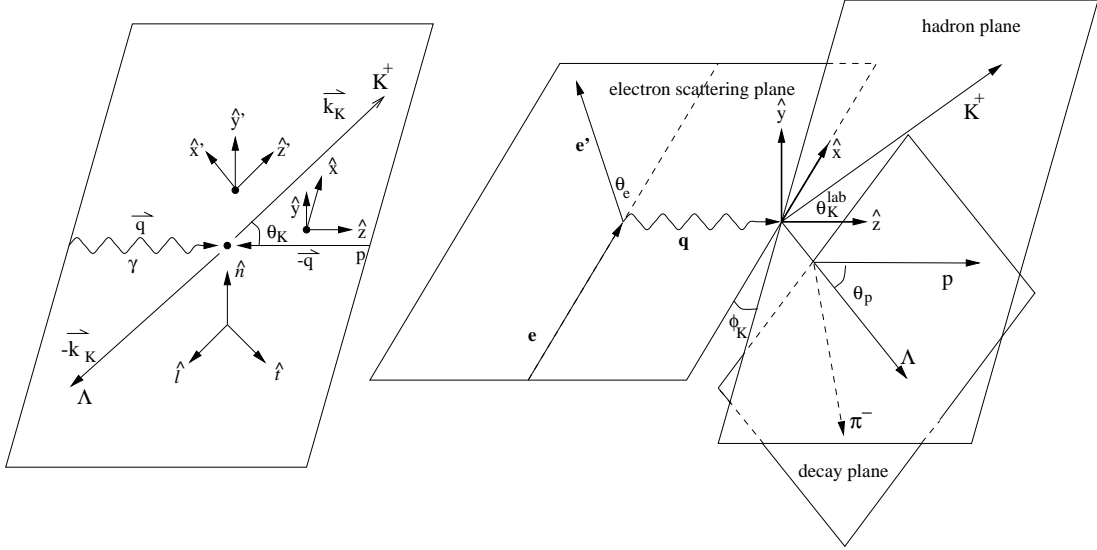


Figure 3: Kinematics for $K\Lambda$ electroproduction showing angles and polarization axes in the c.m. (left) and lab (right) reference frames.

The polarization-projection operators are defined as

$$\begin{aligned} S_\alpha &= (1, \mathbf{S}) \\ S_\beta &= (1, \mathbf{S}') \end{aligned}$$

with

$$\begin{aligned} \mathbf{S} &= (\hat{S}_x, \hat{S}_y, \hat{S}_z) \\ \mathbf{S}' &= (\hat{S}_{x'}, \hat{S}_{y'}, \hat{S}_{z'}). \end{aligned}$$

The unprimed-coordinate system (electron-plane coordinates) is defined such that \hat{z} is along \vec{q} , \hat{y} is normal to the electron-scattering plane, and $\hat{x} = \hat{y} \times \hat{z}$. The primed-coordinate system (hadron-plane coordinates) is defined such that \hat{z}' is along the kaon momentum vector \vec{k}_K , \hat{y}' is normal to the hadronic plane, and $\hat{x}' = \hat{y}' \times \hat{z}'$.

In the case where there is no beam, target, or recoil polarization, Eq. 2 reduces to

$$\sigma_0 \equiv \left(\frac{d\sigma_\nu}{d\Omega_K} \right)^{00} = K \left[R_T^{00} + \epsilon_L R_L^{00} + \sqrt{2\epsilon_L(1+\epsilon)} R_{TL}^{00} \cos \phi_K + \epsilon R_{TT}^{00} \cos 2\phi_K \right] \quad (3)$$

so that $KR_i^{00} = \sigma_i$ of the usual unpolarized cross-section notation.

In the case of a polarized electron beam incident on an unpolarized target producing a polarized recoil, Eq. 2 becomes

$$\frac{d\sigma_\nu}{d\Omega_K} = \sigma_0(1 + hA_{TL'} + P_{x'}\hat{S}_{x'} + P_{y'}\hat{S}_{y'} + P_{z'}\hat{S}_{z'}) \quad (4)$$

where

$$A_{TL'} = \frac{K}{\sigma_0}\sqrt{2\epsilon_L(1-\epsilon)}R_{TL}^{00}\sin\phi_K.$$

The terms $P_{j'} = P_{j'}^0 + hP_{j'}'$, where $P_{j'}^0$ corresponds to the *induced* polarization of the Λ , and $P_{j'}'$ corresponds to the *transferred* polarization. They are written in terms of the response functions as:

$$\begin{aligned} P_{x'}^0 &= \frac{K}{\sigma_0}\left(\sqrt{2\epsilon_L(1+\epsilon)}R_{TL}^{x'0}\sin\phi_K + \epsilon R_{TT}^{x'0}\sin 2\phi_K\right) \\ P_{y'}^0 &= \frac{K}{\sigma_0}\left(R_T^{y'0} + \epsilon_L R_L^{y'0} + \sqrt{2\epsilon_L(1+\epsilon)}R_{TL}^{y'0}\cos\phi_K + \epsilon R_{TT}^{y'0}\cos 2\phi_K\right) \\ P_{z'}^0 &= \frac{K}{\sigma_0}\left(\sqrt{2\epsilon_L(1+\epsilon)}R_{TL}^{z'0}\sin\phi_K + \epsilon R_{TT}^{z'0}\sin 2\phi_K\right) \\ P_{x'}' &= \frac{K}{\sigma_0}\left(\sqrt{2\epsilon_L(1-\epsilon)}R_{TL'}^{x'0}\cos\phi_K + \sqrt{1-\epsilon^2}R_{TT'}^{x'0}\right) \\ P_{y'}' &= \frac{K}{\sigma_0}\sqrt{2\epsilon_L(1-\epsilon)}R_{TL'}^{y'0}\sin\phi_K \\ P_{z'}' &= \frac{K}{\sigma_0}\left(\sqrt{2\epsilon_L(1-\epsilon)}R_{TL'}^{z'0}\cos\phi_K + \sqrt{1-\epsilon^2}R_{TT'}^{z'0}\right). \end{aligned} \quad (5)$$

To accommodate finite bin sizes and to improve statistics, Eq. 4 will need to be integrated over ϕ_K . Therefore, the polarization-projection operators $\hat{S}_{j'}$ need to be written in terms of the coordinates x, y, z . The hadron-plane coordinates are related to the electron-plane coordinates by a counterclockwise rotation of ϕ_K about \hat{z} followed by a counterclockwise rotation of θ_K about \hat{y}' . The rotation matrix which relates the coordinates is

$$\mathcal{R} = \begin{pmatrix} \cos\theta_K \cos\phi_K & \cos\theta_K \sin\phi_K & -\sin\theta_K \\ -\sin\phi_K & \cos\phi_K & 0 \\ \sin\theta_K \cos\phi_K & \sin\theta_K \sin\phi_K & \cos\theta_K \end{pmatrix}. \quad (6)$$

So that we can define the polarization-projection operator in the electron plane in terms of that of the hadron plane:

$$\mathbf{S}' = \mathcal{R}\mathbf{S} = \begin{pmatrix} \cos\theta_K \cos\phi_K \hat{S}_x + \cos\theta_K \sin\phi_K \hat{S}_y - \sin\theta_K \hat{S}_z \\ -\sin\phi_K \hat{S}_x + \cos\phi_K \hat{S}_y \\ \sin\theta_K \cos\phi_K \hat{S}_x + \sin\theta_K \sin\phi_K \hat{S}_y + \cos\theta_K \hat{S}_z \end{pmatrix} \quad (7)$$

Using these relationships for \hat{S}_j , the cross section can be rewritten as

$$\frac{d\sigma_\nu}{d\Omega_K} = \sigma_0(1 + hA_{TL'} + P_x\hat{S}_x + P_y\hat{S}_y + P_z\hat{S}_z) \quad (8)$$

where $P_j = P_j^0 + hP_j'$ with

$$\begin{aligned} P_x^0 &= P_{x'}^0 \cos \theta_K \cos \phi_K + P_{y'}^0 (-\sin \phi_K) + P_{z'}^0 \sin \theta_K \cos \phi_K \\ P_y^0 &= P_{x'}^0 \cos \theta_K \sin \phi_K + P_{y'}^0 \cos \phi_K + P_{z'}^0 \sin \theta_K \sin \phi_K \\ P_z^0 &= P_{x'}^0 (-\sin \theta_K) + P_{z'}^0 \cos \theta_K \\ P_x' &= P_{x'}' \cos \theta_K \cos \phi_K + P_{y'}' (-\sin \phi_K) + P_{z'}' \sin \theta_K \cos \phi_K \\ P_y' &= P_{x'}' \cos \theta_K \sin \phi_K + P_{y'}' \cos \phi_K + P_{z'}' \sin \theta_K \sin \phi_K \\ P_z' &= P_{x'}' (-\sin \theta_K) + P_{z'}' \cos \theta_K. \end{aligned} \quad (9)$$

These are now the observed induced (P_j^0) and transferred (P_j') polarizations of the Λ s measured with respect to electron-plane coordinate system.

The cross section becomes greatly simplified for ϕ_K integrated from 0 to 2π resulting in

$$\int_0^{2\pi} \frac{d\sigma_\nu}{d\Omega_K} d\phi_k = \left(\int \sigma_0 \right) (1 + \mathcal{P}_x S_x + \mathcal{P}_y S_y + \mathcal{P}_z S_z) \quad (10)$$

where

$$\int \sigma_0 = 2\pi K (R_T^{00} + \epsilon_L R_L^{00}) \quad (11)$$

and

$$\mathcal{P}_j = \mathcal{P}_j^0 + h\mathcal{P}_j'. \quad (12)$$

The individual \mathcal{P}_j are

$$\begin{aligned} \mathcal{P}_x^0 &= 0 \\ \mathcal{P}_x' &= \pi \sqrt{2\epsilon_L(1-\epsilon)} \frac{K}{\int \sigma_0} (R_{TL'}^{x'0} \cos \theta_K - R_{TL'}^{y'0} + R_{TL'}^{z'0} \sin \theta_K) \\ \mathcal{P}_y^0 &= \pi \sqrt{2\epsilon_L(1+\epsilon)} \frac{K}{\int \sigma_0} (R_{TL}^{x'0} \cos \theta_K + R_{TL}^{y'0} + R_{TL}^{z'0} \sin \theta_K) \\ \mathcal{P}_y' &= 0 \\ \mathcal{P}_z^0 &= 0 \\ \mathcal{P}_z' &= 2\pi \sqrt{1-\epsilon^2} \frac{K}{\int \sigma_0} (-R_{TT'}^{x'0} \sin \theta_K + R_{TT'}^{z'0} \cos \theta_K). \end{aligned} \quad (13)$$

We see that only the induced parts of the polarization survive for P_y and only the transferred parts for P_x and P_z . These observables (plotted in Fig. 7, 8, and 9) are the primary focus of this experiment. Other response functions can be accessed by different ϕ -binning of the data but will not be determined as well as those in Eq. 13 due to limited statistical accuracy.

2.2 Hadrodynamic Models

Fig. 4 shows the unpolarized cross section $\frac{d\sigma}{d\Omega_K} = \sigma_T + \epsilon\sigma_L$ for $ep \rightarrow e'K^+\Lambda$. The curves are hadrodynamic-model calculations [2] in which two different baryon form factors have been used in combination with three different forms of the t -channel exchange particles (K, K^* , and $K1$). The figure shows that the unpolarized cross section is not significantly sensitive to the different kaon form factors included in the calculations of Ref. [2]. The importance of cross section measurements should not be understated however. Fig. 5 shows the results of the LT separation measurement of Niculescu *et al.* [8] in which the data exhibit rather pronounced differences from the calculations especially at large Q^2 where the results of the calculations are above the upper limit of the plot.

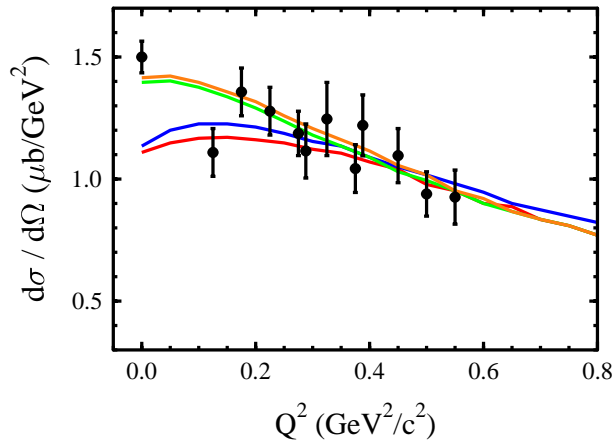


Figure 4: Differential cross section $d\sigma/d\Omega_K = \sigma_T + \epsilon\sigma_L$ as a function of Q^2 for $ep \rightarrow e'K^+\Lambda$ at $\epsilon = 0.72$, $s = 5.02(\text{GeV}/c)^2$, $t = -0.15(\text{GeV}/c)^2$. Data are from Ref. [17] while curves are from Ref. [2] and are described in the text.

Some single-polarization observables are expected to show a strong model dependence. Fig. 6 [2] shows the three single-polarization observables (Λ -polarization

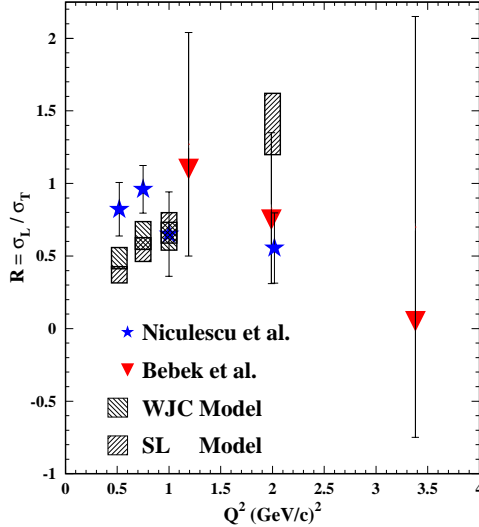


Figure 5: The ratio $R = \sigma_L/\sigma_T$ for $ep \rightarrow e'K^+\Lambda$ at $W = 2.15$ GeV from Ref [8] and Ref. [18] with calculations from Ref. [2] and Ref [3].

asymmetry; $P = R_T^{y^0}/R_T^{00}$, polarized target asymmetry; $T = R_T^{0y}/R_T^{00}$, and linearly polarized beam asymmetry; $\Sigma = -^c R_{TT}^{00}/R_T^{00}$) for *photoproduction* as a function of photon energy. We first note the relative sparsity of data. No data exists for Σ and the data for P and T cover only a small portion of the energy range where these calculations are expected to be valid. Furthermore, there is little disagreement between the models in the range of the existing data. Currently approved JLab experiments E89-004 [11] (photoproduction) and E89-043 [12] (electroproduction) will measure the induced polarization of the outgoing Λ to expand the existing data base.

Fig. 7 shows \mathcal{P}_z at 4.0 GeV and $\theta_K = 90^\circ$ as a function of Q^2 for $W = 1.7, 1.9,$ and 2.1 GeV using different choices of model and Λ form factor. The curves are hadrodynamical-model calculations from code provided by T. Mart [21] which outputs response functions that are then used to calculate our observables. The model choices are Adelseck and Wright (AW); Cotanch (C); Williams, Ji, and Cotanch (WJC); Mart 1, 2, and 3 (M1, M2, M3). Lambda form factors are dipole (D); set to 1 (1); Williams, Ji, and Cotanch 1, 2, 3 (W1, W2, W3); and Goeke (G). Variations in the $K^+K^{*+}\gamma$ -transition form factor are also made (though not shown here) using form factors from VMD; Muenz (M); and Williams, Ji, and Cotanch (w1). We see a strong sensitivity to both choice of model and Λ

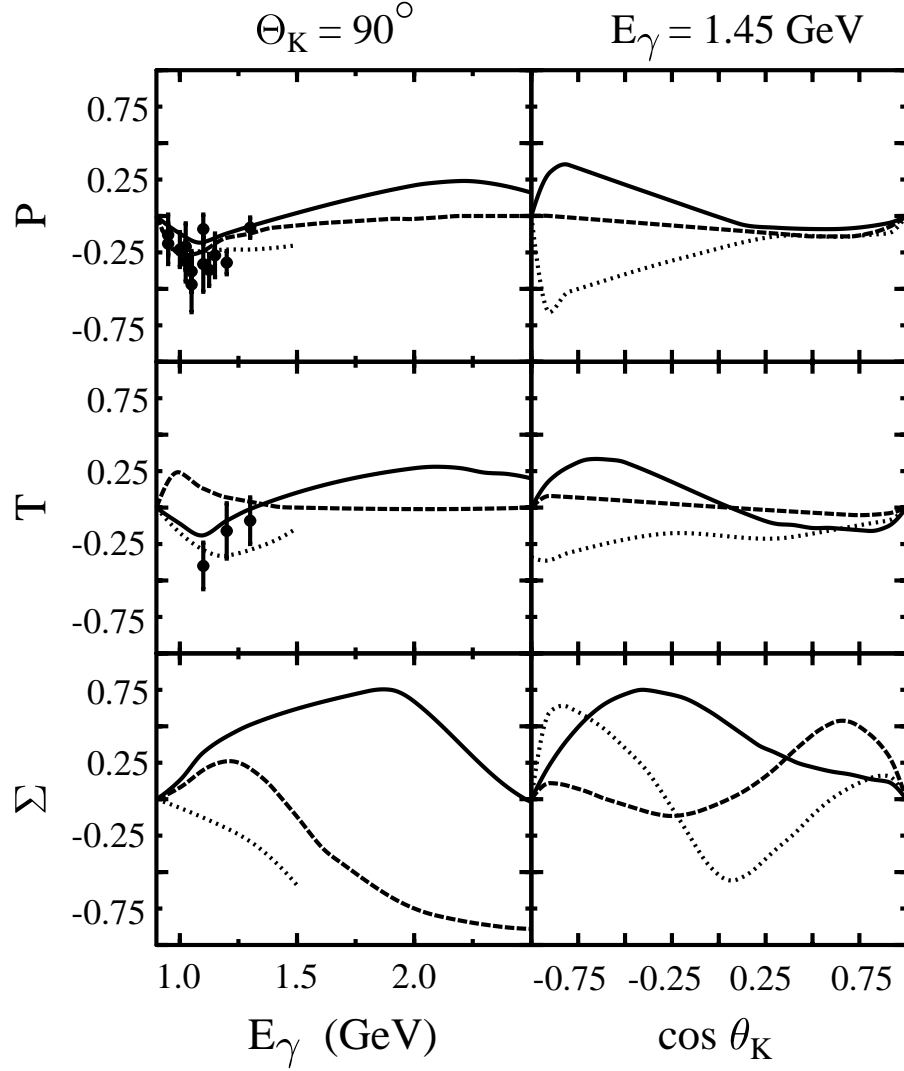


Figure 6: Single-polarization observables for Λ -polarization asymmetry P , polarized target asymmetry T , and linearly polarized beam asymmetry Σ for $\gamma p \rightarrow K^+ \Lambda$. Data are from Ref. [19] (P) and Ref. [20] and the curves are from Refs. [1] (dots), [2] (solid), and [3] (long-dash).

form factor. \mathcal{P}_z contains a term with $R_{TT'}^{z'0}$, which by itself is expected to exhibit sensitivity to the Λ -magnetic form factor Ref. [23].

Fig. 8 shows the angular distributions at 4.0 GeV for \mathcal{P}_z at $Q^2 = 1.0$ (GeV/c)² and $W = 1.7, 1.9,$ and 2.1 GeV using different choices of model, Λ form factor, and $K^+K^{*+}\gamma$ -transition form factor. We see that our proposed data are quite sensitive to the three variations of the calculation. It is especially evident that within the choice of the model, that the data will place tight constraints on the $K^+K^{*+}\gamma$ -transition form factor.

Fig. 9 shows the angular distributions for the three double-polarization observables, \mathcal{P}_x , \mathcal{P}_y , and \mathcal{P}_z , of this experiment at $W = 1.7$ GeV and $Q^2 = 1.0$ (GeV/c)². \mathcal{P}_x shows some sensitivity to various choices while \mathcal{P}_z again shows strong sensitivity to all three choices. \mathcal{P}_y shows little sensitivity to model or form factor choices but has been included for completeness. Significant deviations of the data from the calculations for \mathcal{P}_y could indicate flaws in the underlying assumptions of hadrodynamical models.

There have been two important recent breakthroughs regarding the hadrodynamical model calculations for photoproduction that have strengthened the state of the existing calculations. The first is a recent coupled-channels analysis that has included hadronic rescattering for the first time to handle processes such as $\gamma N \rightarrow N^* \rightarrow \pi N \rightarrow N^{**} \rightarrow KY$, where N^* and N^{**} are different nucleon resonances [24]. The second advancement demonstrates how hadronic form factors can be included in a consistent and gauge invariant fashion. This provides the possibility of achieving good fits with a $K\Lambda N$ coupling constant close to SU(3) values [25]. Both advancements are being extended to electroproduction with calculations available in the near future.

2.3 Quark Models

One exciting prospect of this experiment is that it may shed light on quark-production mechanisms. In a naive approach, one can consider the incident polarized virtual photon interacting with one of the two u quarks of the target proton (see Fig. 2a). This process is nearly an order of magnitude more likely than an interaction with the d quark. The struck u quark is then polarized. As the u quark recoils against the correlated ud pair, a “flux-tube”, or color string, is believed to “stretch” between the recoiling quark-diquark system of the decaying N^* resonance until it breaks creating an $s\bar{s}$ pair. Since the K^+ has spin 0, and hence cannot carry polarization, this forces the spin of the \bar{s} quark to be aligned opposite to that of the u quark. Since the spin of the Λ is assumed to be carried entirely by the s quark, then measurement of the Λ polarization can be used to

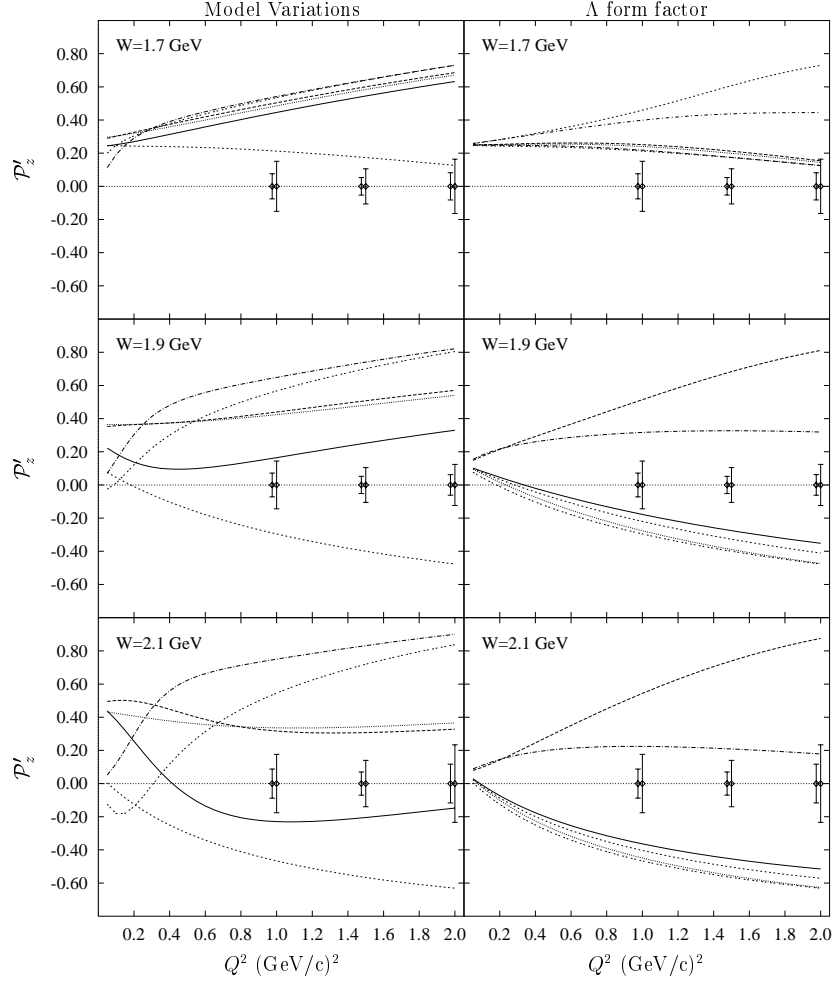


Figure 7: \mathcal{P}'_z at $E = 4.0$ GeV and $\theta_K = 90^\circ$ as a function of Q^2 for $W = 1.7, 1.9,$ and 2.1 GeV and different choices of model (left) and Λ form factor (right). The left column uses Λ form factor G and kaon form factor w1 with models AW (solid), C (long dashes), WJC (short dashes), M1 (dots), M2 (dot-dash), and M3 (dash-dash). The right column uses model WJC, kaon form factor w1, and Λ form factors D (solid), 1 (long dashes), W1 (short dashes), W2 (dots), W3 (dot-dash), and G (dash-dash). The larger experimental uncertainties (statistical only) are what we expect after one month of running and the smaller uncertainties are what we expect after four months.

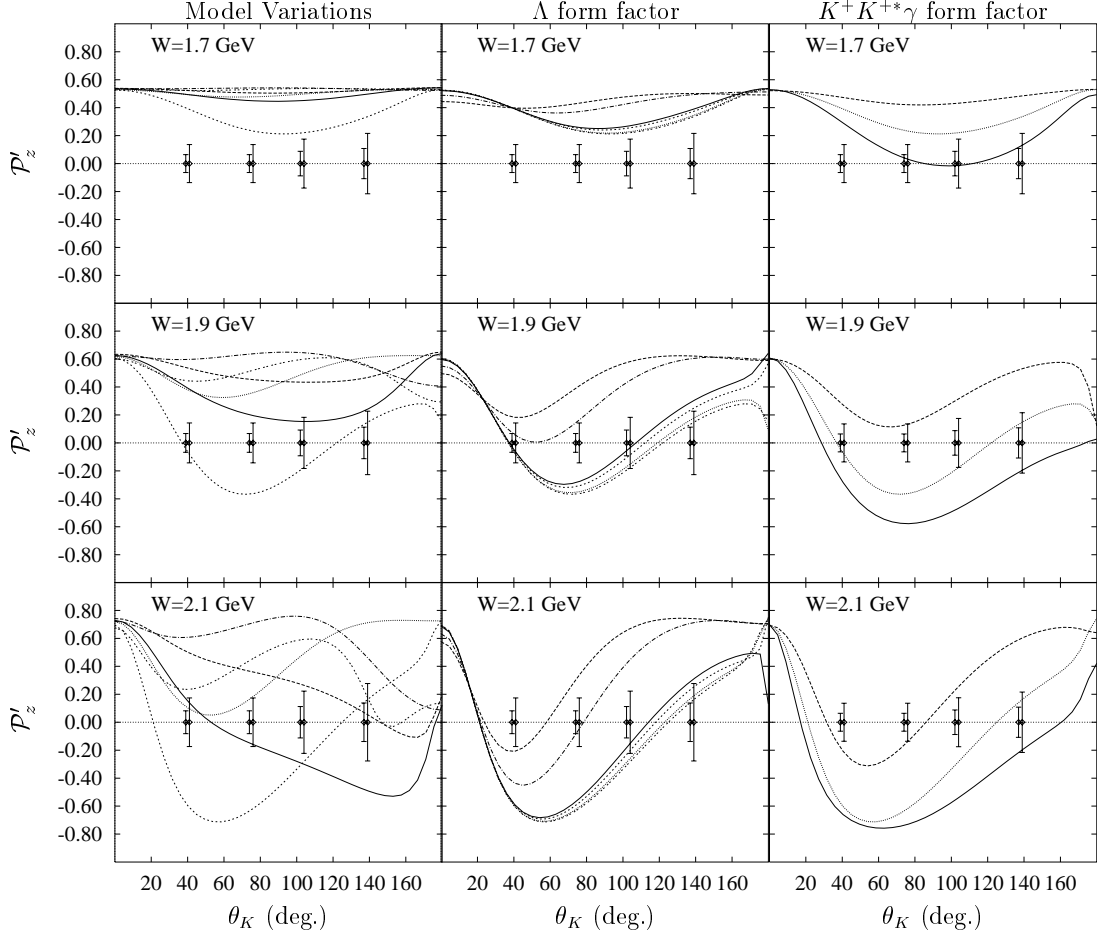


Figure 8: \mathcal{P}'_z as a function of θ_K for different models and form factors at $E = 4.0$ GeV, $W = 1.7, 1.9,$ and 2.1 GeV, and $Q^2 = 1.0$ (GeV/c) 2 . The left column shows model variations (curves same as Fig. 7) and the center column shows Λ form factor variations (curves same as Fig. 7). The right column shows $K^+K^{*+}\gamma$ -transition form factor variations using model WJC, Λ form factor G, and kaon form factors VMD (solid), M (dashes), w1 (dots). The uncertainties are as in Fig. 7.

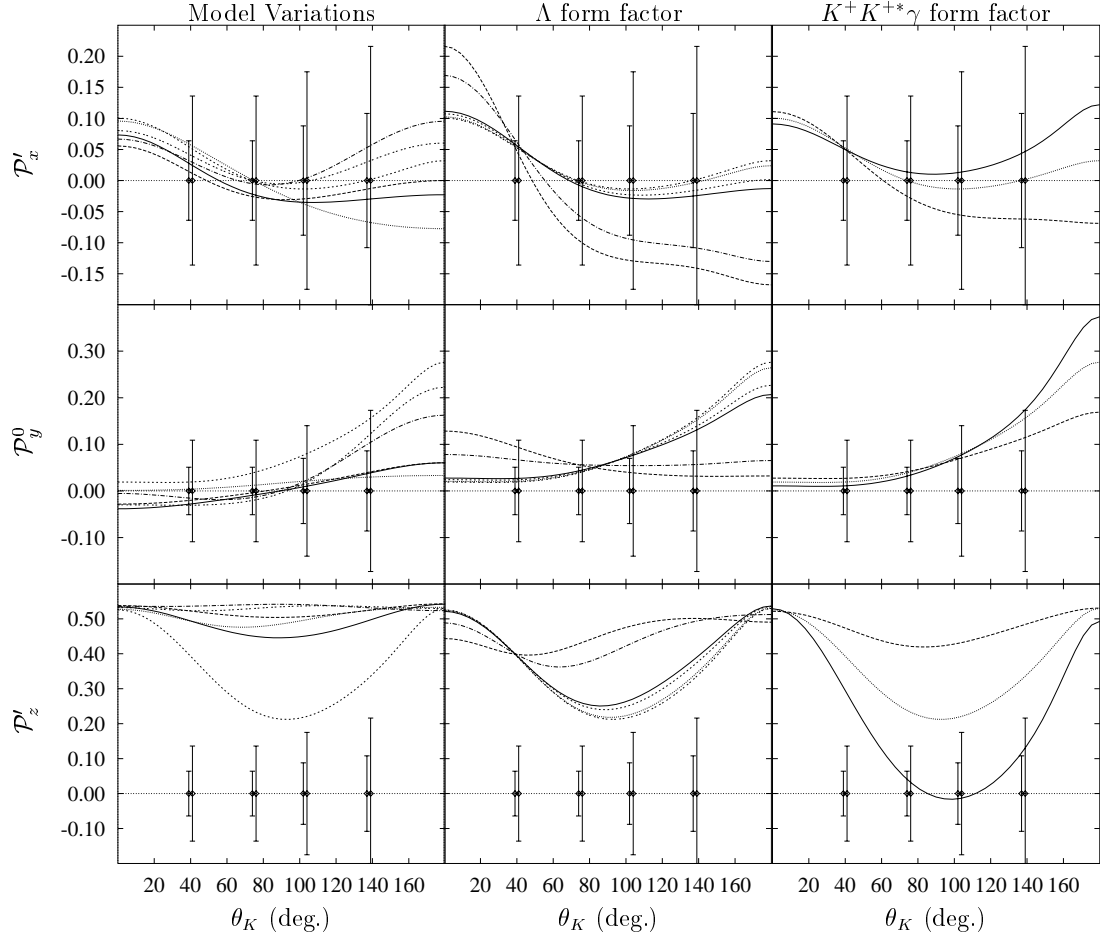


Figure 9: \mathcal{P}_j as a function of θ_K for different models and Λ form factors at $E = 4.0$ GeV, $W = 1.7$ GeV, and $Q^2 = 1.0$ (GeV/c) 2 . The left column shows model variations (curves same as Fig. 7), the center column shows Λ form factor variations (curves same as Fig. 7), and the right column shows $K^+K^{*+}\gamma$ -transition form factor variations (curves same as Fig. 8). The uncertainties are as in Fig. 7.

study the angular momentum of the $s\bar{s}$ pair.

Strong decays of the type $N^* \rightarrow K\Lambda$ are still a rather poorly understood area of hadronic physics. Calculations for this type of coupling are essential to understand the role of strangeness in the standard model, as well as the inter-quark potential. There have been many attempts over the past 30 years to model strong decays through $q\bar{q}$ pair production [4, 26, 27, 28]. However, there is still a fair amount of ambiguity regarding the angular momentum of the $q\bar{q}$ pair created. There have been suggestions that the quark pair should be created with vacuum quantum numbers [27], as well as suggestions that the pair should have quantum numbers of a single gluon [29].

Vacuum quantum numbers correspond to $J^\pi = 0^+$. Since this corresponds to a 3P_0 $q\bar{q}$ state, it is generally referred to as the 3P_0 quark pair creation model. Similarly the single gluon quantum numbers of $J^\pi = 1^-$ correspond to a 3S_1 $q\bar{q}$ state. The 3S_1 quark pair creation model assumes that the $q\bar{q}$ pair came from a single gluon (OGE). Regardless of the quantum numbers of the created quark pair, the fundamental decay mechanism is not understood. It is currently believed to be a non-perturbative process involving flux-tube breaking with the $s\bar{s}$ quark pair “popping” out of the vacuum for the 3P_0 case, or a single gluon “popping” out with a subsequent decay to the $s\bar{s}$ pair.

At the present time the 3P_0 model is more widely accepted than the 3S_1 model due to its success for meson decay (especially the decays $a_1 \rightarrow \omega\pi$, $b_1 \rightarrow \omega\pi$). However, the 3P_0 assumption fails in several cases such as the $f_0 \rightarrow \pi\pi$ channel [28]. It is generally believed that both 3P_0 and 3S_1 mechanisms must be present but that 3P_0 coupling is dominant [30].

Detailed tests of the decay models are therefore important and it is believed that polarization observables provide a sensitive test [27, 31]. The best tests of the decay models will come from final states that clearly result from a single intermediate N^* resonance. This is an important reason to select bins in W to be as narrow as possible (in order to isolate single resonances) or, alternatively, a careful partial wave analysis is required to pull out the resonant amplitudes with a given J^π .

The interpretation of our data must be done within the framework of the models to be tested. Quark models can provide masses of intermediate resonances which need to be coupled with models such as 3P_0 or 3S_1 that provide the strong-decay coupling constants of the baryonic resonances. One then uses a model for the photo-coupling vertices to produce observables such as polarization asymmetries. Any disagreement between theory and the experiment could arise from a number of different sources: the model of the strong decay vertex, the model of the photo-coupling vertex, the momentum dependence at either vertex,

or even the model used to describe the scattering itself.

Despite these model dependencies, polarization observables are important ingredients in any comparison of 3P_0 and 3S_1 models. The decay widths and masses of baryonic resonances with which the models are compared must be obtained from several experiments by means of partial wave analyses. The partial wave analysis cannot be done in any meaningful way without polarization observables. Furthermore, these observables must be taken over as large a range of phase space as possible. This is best done using a large acceptance detector such as CLAS.

2.4 Regge Theory

Meson photo- and electroproduction data for the reaction $\gamma^{(*)}p \rightarrow \pi N$ have been compared with a new model based on a Regge description [15]. At intermediate energies ($E_\gamma \geq 4$ GeV) and intermediate momentum transfers ($-t \leq 3$ (GeV/c) 2), a Regge trajectory exchange model has proven to be superior to Born-diagram models [32, 33] when compared to the available published cross section and asymmetry data. The model has recently been extended to study $K^+\Lambda$ and $K^+\Sigma^0$ electroproduction in these same kinematics (above the resonance region at low $-t$), with coupling constants determined from kaon photoproduction reactions [5]. This gauge invariant model provided a good description of the available unpolarized and polarized photoproduction data. Fig. 10 shows the results for the $\gamma^*p \rightarrow K^+\Lambda$ forward differential cross section as a function of Q^2 at $W \sim 2.15$ GeV. A monopole parameterization of the kaon form factor with $\Lambda_K^2 = \Lambda_{K^*}^2 = 0.6$ GeV 2 has been used.

Starting from a standard Feynman-diagram formalism, the exchange of a Regge trajectory is accomplished by replacing the usual pole-like Feynman propagator of a single particle (i.e. $1/(t - m^2)$, where m is the mass of the exchanged particle) by a so-called Regge propagator. The Regge propagator represents a family of particles all with the same internal quantum numbers. The model is simple in that it is based on the K and K^* Regge exchanges in the t -channel. s -channel Born diagrams are included to preserve gauge invariance. In previous Regge models, the cross sections were predicted only after inclusion of non-physical “over-absorption” [34], however, the current model reproduces both unpolarized and polarized observables over the full energy range of the existing data.

It is expected that detailed comparisons of this model to the observables of electroproduction (cross sections and polarization observables) will help to quantify the transition from the non-perturbative to perturbative QCD (pQCD) regimes. An extrapolation of the Regge model to momentum transfers where

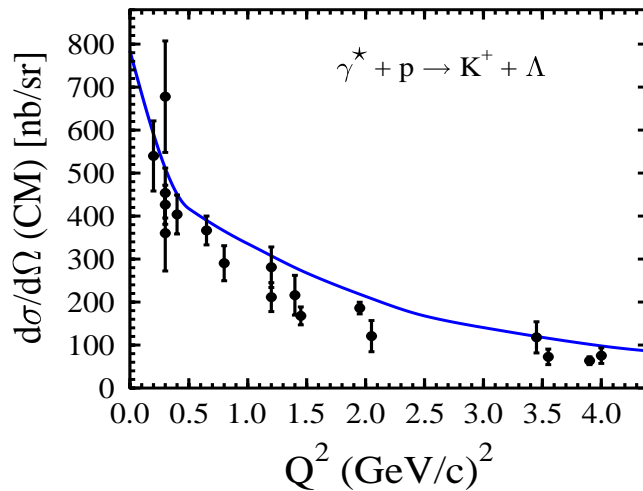


Figure 10: Differential cross section for $\gamma^*p \rightarrow K^+\Lambda$ at $W = 2.15$ GeV, $\epsilon = 0.85$, and averaged over forward angles ($\theta_K < 15^\circ$) [5].

pQCD is valid has been performed for the pion photoproduction reaction with good results [5, 15]. Similar extrapolations are planned for the kaon photo- and electroproduction reactions [35]. Data at these kinematics are particularly sparse. Therefore, measurements of kaon electroproduction observables above the resonance region at CEBAF energies ($E_\gamma : 4 \rightarrow 6$ GeV) are necessary for the development of theoretical models that bridge the transition region [35].

Regge calculations [35] of P_x , P_y , and P_z are presented in Fig. 11 for a beam energy of 4.0 GeV with $W = 1.8$ GeV and $Q^2 = 1.0$ (GeV/c)² at $\phi_K = 180^\circ$ along with results for the hydrodynamic-model calculation WJC. At the present time, no calculation of the observables \mathcal{P}_j exist. However, the striking differences between the two types of calculations for these observables suggest that our double polarization observable data will be a valuable tool for selecting model preference.

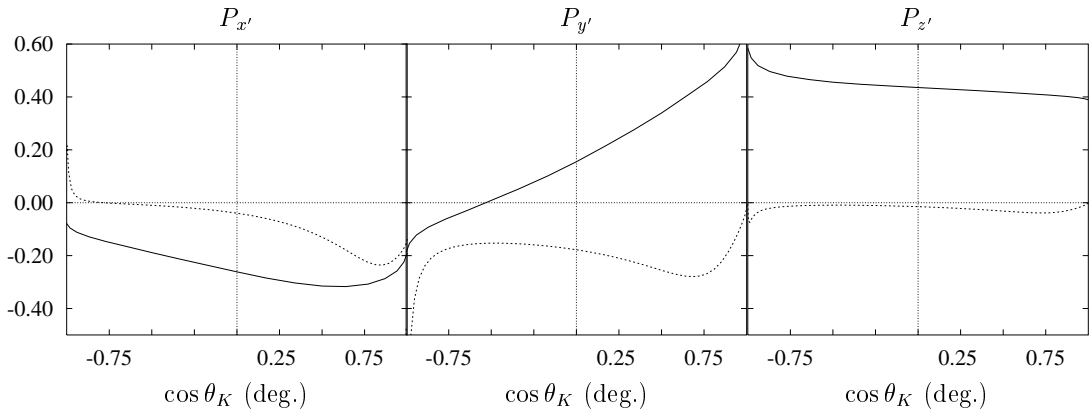


Figure 11: Regge exchange calculation (solid curves) for Λ electroproduction [36] double-polarization observables as defined in Eq. 5. The calculation is done for a 4.0 GeV beam energy with $W = 1.8$ GeV and $Q^2 = 1.0$ (GeV/c) 2 at $\phi_K = 180^\circ$. For comparison, the hadrodynamic-model calculation WJC has been included.

3 Experimental Overview

We present in this section our plans for studying the electroproduction of Λ hyperons from a hydrogen target using a longitudinally polarized electron (circularly polarized virtual photon) beam. We propose to take data using the CLAS spectrometer with the polarity chosen such that the electrons are bent towards the beam axis. The main goal of our study is to measure the Λ -hyperon polarization components, thus we must directly detect the inelastically scattered electron, the produced K^+ meson, and the decay proton from the associated Λ (B.R.=0.639 for $\Lambda \rightarrow p\pi^-$). The protons from the decay are constrained to move preferentially in the direction of the Λ spin, thus measuring the proton angular correlation allows determination of the Λ polarization.

The kinematics of the γ^*p interaction are determined by three independent kinematical variables, usually chosen to be the “mass” of the virtual photon Q^2 , the total center-of-mass (CM) energy W (or equivalently the mass of the excited intermediate resonance), and the kaon scattering angle in the resonance CM system θ_K . Our data at each beam energy will be binned in these variables in addition to ϕ_K .

We propose to collect data at 2.4 and 4.0 GeV in the full Q^2 and W acceptance of CLAS as shown in Fig. 12. Our bins will span a range of W from 1.6 to 2.4 GeV and Q^2 from 0.4 to 2.7 (GeV/c)². Our proposed energy bins are highlighted by the overlaid grid pattern. The lower limit on W is imposed by the $K-\Lambda$ production threshold. We will measure the electron beam helicity dependent and independent components of the Λ polarization over the full range of t spanned by CLAS.

We have planned this experiment to be compatible with other experiments measuring electroproduction on hydrogen. These experiments, in the so-called e1 run group, all employ a minimum bias trigger based on detecting a scattered electron in one of the forward electromagnetic calorimeters. By measuring the 3-momenta of both the electron and charged K^+ , we will be able to bin each event uniquely according to its value of Q^2 , W , $\cos\theta_K$, and ϕ_K for each beam energy.

The first portion of the e1 data ($\sim 10\%$ of the allotted total) was acquired with an unpolarized electron beam incident upon the Hall B liquid hydrogen target in the period from December 1997 to March 1998. This has provided us with a particularly unique opportunity to analyze this data to eliminate essentially all major uncertainties in the expected data rates for our Q^2 and W bins. This has greatly solidified our understanding of the statistical uncertainties that we can achieve at these beam energies.

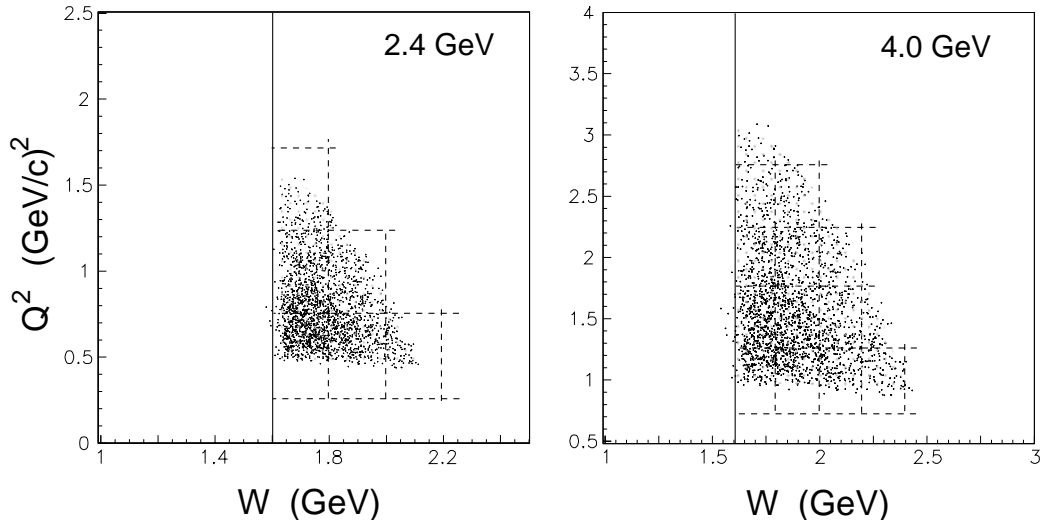


Figure 12: Q^2 and W bins selected for this experiment at 2.4 and 4.0 GeV. Q^2 binned in ± 0.25 $(\text{GeV}/c)^2$ and W binned in ± 0.1 GeV. The lower limit on the acceptable W is 1.6 GeV corresponding to the $K - \Lambda$ threshold. Each box represents one of our data bins.

In the following subsections more details are provided about the acceptance for the three body final state of interest within the CLAS detector, the expected statistical uncertainties for our choice of energy and angle bins, particle identification and backgrounds, as well as estimates of the expected systematic uncertainties. Also a section is provided to illustrate exactly how the polarization observables will be extracted from the collected data.

3.1 CLAS Acceptance Studies

3.1.1 Electron Kinematics and Acceptance Limits

The scattered electrons of interest in this reaction are cleanly detected within the volume of the forward calorimeters. They provide a very clear signature since they are negatively charged particles moving with essentially $\beta = 1$. To detect an electron within CLAS, it must traverse the drift chambers and Čerenkov counters, and hit the face of the electromagnetic calorimeters. The region of momentum and scattering angle for which the electrons are detected is shown in Fig. 13 for beam energies of 2.4 and 4.0 GeV and with the main CLAS toroid set with

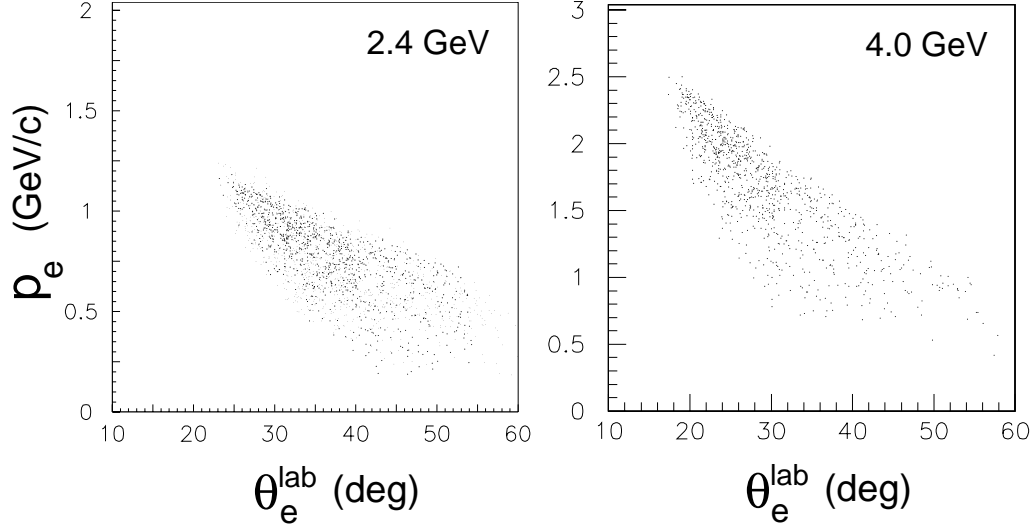


Figure 13: Electron acceptance limits in the CLAS detector at beam energies of 2.4 and 4.0 GeV in laboratory angle vs. momentum with the torus bending negatively charged particles bending in towards the beam axis.

polarity corresponding to bending electrons towards the beam axis. The 2.4 GeV data was acquired with the main torus at approximately half field and the 4.0 GeV data was acquired at approximately full field.

To illustrate the experimental conditions in more detail, Fig. 14 shows the range of virtual photon polarization, ϵ , spanned by this proposal as a function of our bins in Q^2 and W . In these plots the upper ϵ limit is set by the maximum beam energy and the lower limit by the maximum electron scattering angle accepted by CLAS. The lower limit on Q^2 is set by the geometric limits on electron acceptance. In order to best understand the Q^2 and W dependence of the Λ polarization, it is important to span the largest possible range of these quantities at each beam energy. The CLAS detector is therefore well suited for this type of measurement. By comparison, the Hall C experiment [13] will take data at seven values of Q^2 ranging from 0.5 to 2.0 (GeV/c)² but with an essentially fixed value for W of 1.67 GeV and a single angle of $\theta_K = 0^\circ$.

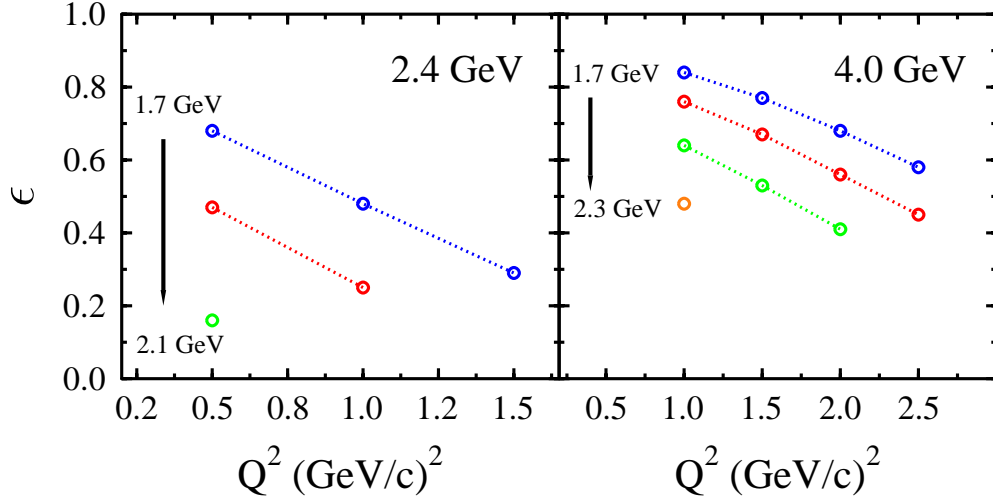


Figure 14: Acceptance of the scattered electron plotted as virtual photon polarization ϵ vs. Q^2 for 2.4 and 4.0 GeV. Each curve or single point represents one of our bins in W .

3.1.2 Kaon Kinematics and Acceptance Limits

The CLAS spectrometer has a large acceptance for the detection of outgoing positive particles, such as the K^+ . This can be seen through an analysis of the existing 2.4 and 4.0 GeV e1 data in Fig. 15 in which the laboratory acceptance limits for kaon detection are plotted versus kaon momentum (p_K) and angle (θ_K^{lab}). This plot only includes those reconstructed kaons which traverse all three regions of the drift chambers and strike the scintillation counters. Kaons with low momentum are curled up by the magnetic field and fail to reach the scintillators, while those with small production angles and large momentum end up in the forward hole of the toroid. In this first-order analysis, kaons that decay in flight before detection are not reconstructed. Those that do not decay in flight can be positively identified by a measurement of their β , or rather, their flight time from the target to the outer scintillation counters. The separation of kaons and pions is aided by the 50 ps timing resolution.

Fig. 16 illustrates the acceptance and efficiency for kaon detection as a function of CM variables, $\cos \theta_K$ and ϕ_K . As shown shown in Fig. 16a, CLAS subtends the full range of $\cos \theta_K$. The fall off at large angles is due to the combined effects of CLAS geometrical acceptance, kaon in-flight decays, the kaon low momentum

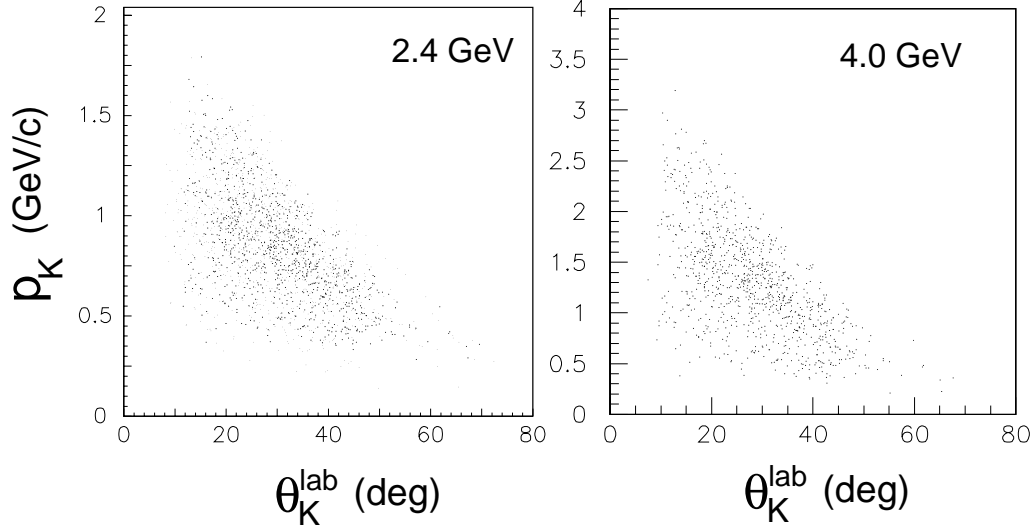


Figure 15: Acceptance of the produced kaons plotted as laboratory momentum vs. angle. Data are extracted from 2.4 and 4.0 GeV e1 data. These kaons represent those that traverse the drift chambers and reach the outer scintillators.

cut-off, and the cross section of the reaction. Fig. 16b is a plot of kaon CM angle versus laboratory angle showing that CLAS is sensitive to kaons out to roughly 60° in the laboratory. For $\theta_K^{lab} \geq 60^\circ$, the kaons have momentum $p_K \leq 300$ MeV/c, and are curled up in the magnetic field and never reach the scintillators.

An important factor reducing our statistical precision by about 50% is the loss of kaons by decay in flight between the target and the scintillators. The typical kaon flight path is about 5.0 m to the scintillators, while their decay length, $c\tau_K$, is 3.0 m. This loss of kaons is highlighted in Fig. 16c. Of course during analysis, this efficiency loss must be taken into account when determining the Λ polarization. There is hope of recovering some of these decay kaons ($K^+ \rightarrow \mu^+ \nu_\mu$ B.R.=64%, $K^+ \rightarrow \pi^+ \pi^0$ B.R.=21%) with improvements and modifications to the existing tracking code by looking for ‘kinks’ in the charged particle tracks. This work is still in its infancy [38].

3.1.3 Proton Kinematics and Acceptance Limits

The polarization of the produced Λ hyperon in a given kinematic bin can be determined through the angular distribution of the decay protons in the Λ rest

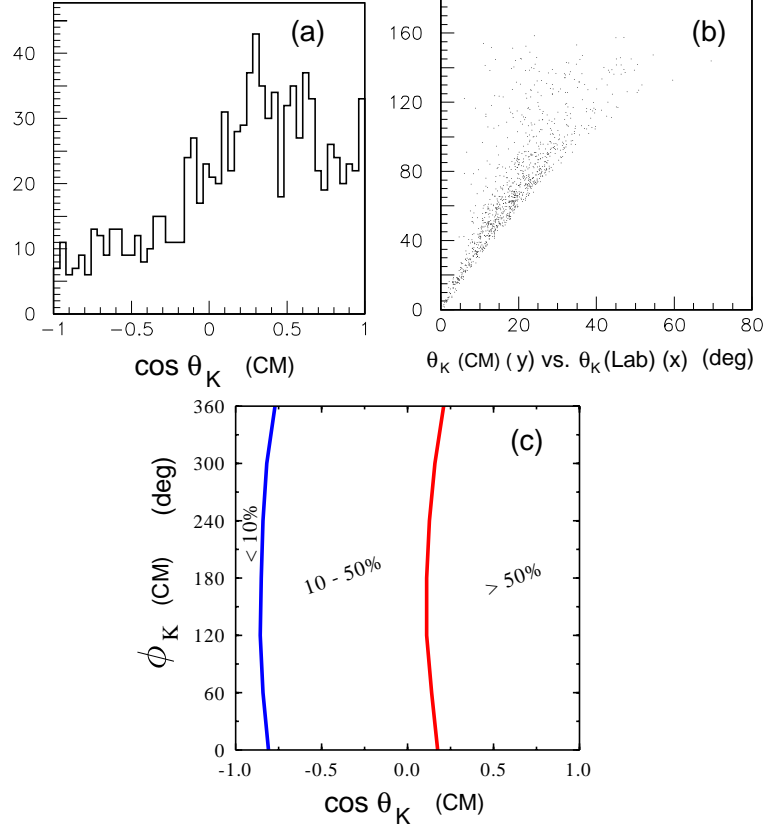


Figure 16: (a). $\cos \theta_K$ distribution from 4.0 GeV data analysis, (b). θ_K^{lab} vs. θ_K , (c). Probability that kaon does not decay before reaching the scintillation counters.

frame (RF) via:

$$\frac{dN}{d\Omega_p} \propto 1 + \alpha P_\Lambda \cos \theta_p^{RF} \quad (14)$$

where θ_p^{RF} is the angle between the hyperon momentum vector in the laboratory frame and the decay proton momentum vector in the Λ rest frame.

The decay protons are constrained to lie in a cone about the direction of the Λ momentum as seen from the p_Λ versus $\theta_{p\Lambda}$ plots in Fig. 17. The size of this cone is dictated by the magnitude of the Λ momentum. Employing the CLAS detector, this cone is fully intercepted over the entire Q^2/W range proposed. The proton kinematics in laboratory momentum and angle are also shown in Fig. 17. Studies of the induced Λ polarization data from the unpolarized 4.0 GeV e1 run are discussed in Sec. 4 to highlight the analysis techniques and systematic uncertainties.

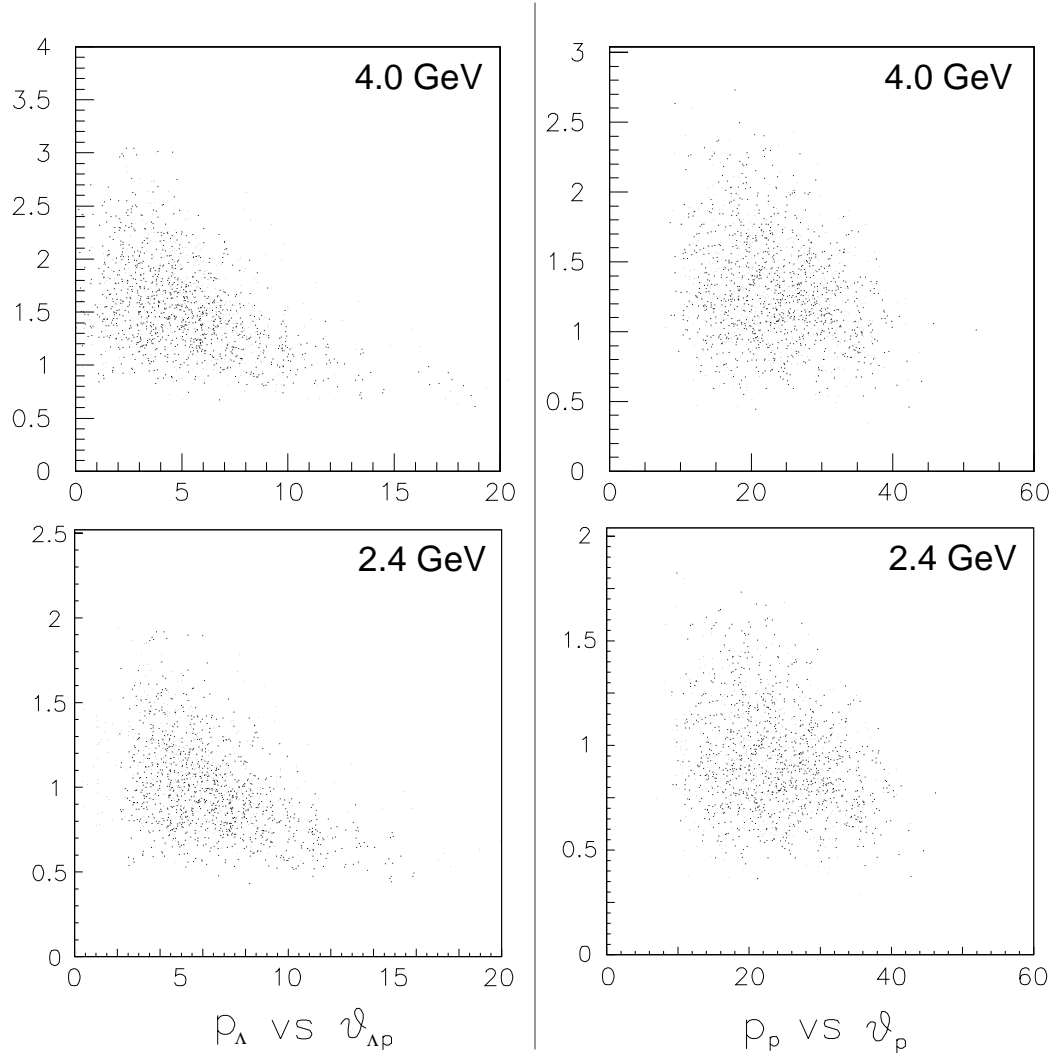


Figure 17: Left: Λ hyperon momentum vs. $\theta_{\Lambda p}$ showing the size of the proton decay cone in the laboratory. Right: Acceptance of the decay protons plotted as the proton-laboratory momentum vs. angle. Plots are from analysis of the 2.4 and 4.0 GeV e1 data.

3.2 Particle Identification and Backgrounds

The main source of background beneath our Λ missing mass peak comes from pions misidentified as kaons. These pions come from the reaction $ep \rightarrow e'\pi^+\Delta^0$. If the pion in this reaction is misidentified as a kaon, the resultant $ep \rightarrow e'K^+X$ missing mass distribution will have an overlapping contamination from this process. However, the 120 MeV width of the Δ^0 implies that this background will be much broader than the CLAS resolution-smeared Λ missing-mass peak. This background has been studied in the 2.4 and 4.0 GeV data. It has been found that the majority of these background pions can be eliminated with suitable cuts as shown in Fig. 18. The sub-plots in this figure highlight the missing-mass distributions with several different cuts imposed. It is clearly seen that reconstructing the missing mass for $p(e, e'K^+)X$ with a cut on the π^- mass from the reconstructed $p(e, e'K^+p)X$ distribution results in a very clean spectrum with essentially only the Λ and Σ^0 peak remaining. The Λ s of interest are then selected with a cut on this last distribution.

Of course, the Λ peak will have a contamination from the Σ^0 peak. The higher the beam energy the worse the energy resolution of CLAS, and the greater this overlap becomes. Currently, there is about a 15% contamination in the Λ peak from the Σ^0 s which will have to be corrected. This is addressed in Sec. 5.

3.3 Data Binning and Statistical Precision

Our full list of proposed bins in Q^2 and W at 2.4 and 4.0 GeV are shown in Table 1. The broad range of kinematic coverage is simply not possible with any other detection system. The expected data rates in each of our Q^2 and W bins for the final state of interest have been studied with the e1 data already acquired. The extracted rates were then used to estimate the statistical uncertainties that we can expect on our Λ -polarization measurements. In determining the expected statistical uncertainties, we have based our calculations on running for 30 days at each energy. This was done with the expectation of approximately 30 days of 4.0 GeV polarized running in the early 1999 e1 running period and a similar amount of time was considered for 2.4 GeV running. For each additional 30 day running period at the same energy, the same torus field setting, and 80% incident electron beam polarization, our total counts can be expected to double, thus reducing the statistical uncertainties on our Λ polarization measurement by about 30%/month.

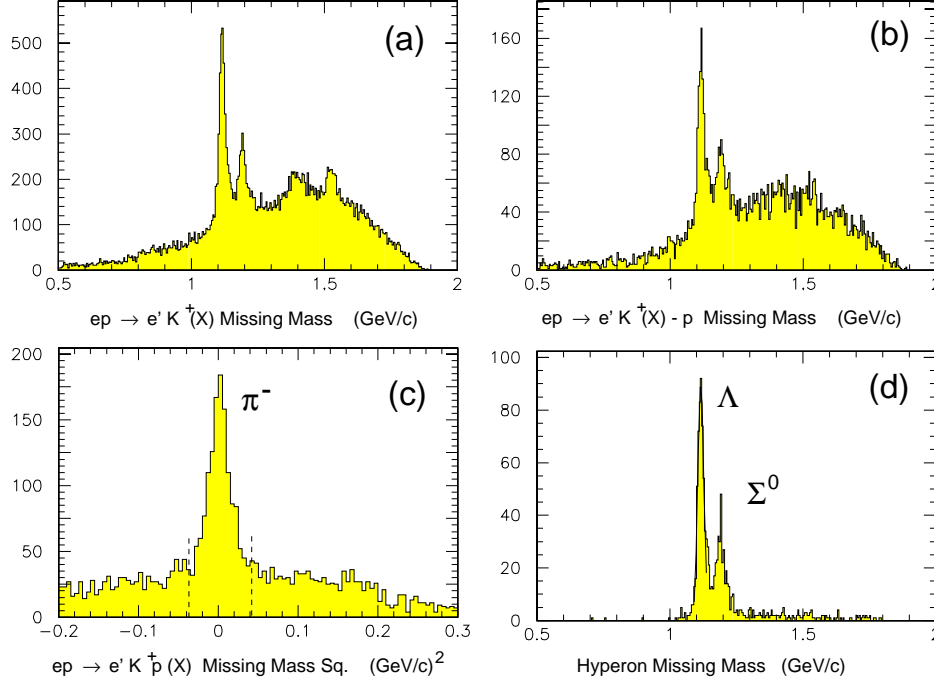


Figure 18: Missing-mass reconstructions for the Λ and Σ^0 from 4.0 GeV CLAS data. (a). M.M. for $p(e, e'K^+)X$, (b). M.M. for $p(e, e'K^+)X$ (with detection of proton), (c). M.M.² for $p(e, e'K^+p)X$ reconstructing the π^- from the Λ decay with cuts shown, (d). Same as (a) with π^- M.M.² cut. The tail at large W is the radiative tail.

The Λ polarization components are defined as:

$$P_{\ell,n,t} = \frac{2}{\eta\alpha} \cdot \frac{N_+ - N_-}{N_+ + N_-} \quad (15)$$

In this expression, η represents the electron beam polarization and α represents the analyzing power of the parity violating weak decay of the Λ ($\alpha = 0.642 \pm 0.013$ [39]). The total number of Λ decay protons detected is $N_0 = N_+ + N_-$. The number of protons in the Λ rest frame going forward and backwards (relative to the coordinate being considered) is given by N_+ and N_- , respectively.

The statistical uncertainty on each component is then given by:

$$\sigma_{P_\Lambda} = \frac{2}{\alpha\eta\sqrt{N_0}} \cdot \left(1 - \frac{1}{4}\alpha^2 P_\Lambda^2\right)^{1/2} \quad (16)$$

4.0 GeV Data Bins						
No.	Q^2	W	ϵ	p_e	θ_e	θ_γ
1	1.0	1.7	0.84	2.40	18.6	23.8
2	1.5	1.7	0.77	2.13	24.2	23.0
3	2.0	1.7	0.68	1.86	30.0	21.3
4	2.5	1.7	0.58	1.60	36.5	19.3
5	1.0	1.9	0.76	2.01	20.3	18.3
6	1.5	1.9	0.67	1.75	26.8	17.9
7	2.0	1.9	0.56	1.48	33.8	16.5
8	2.5	1.9	0.45	1.21	42.1	14.7
9	1.0	2.1	0.64	1.59	22.9	13.7
10	1.5	2.1	0.53	1.32	30.9	13.3
11	2.0	2.1	0.41	1.05	40.3	12.0
12	1.0	2.3	0.48	1.12	27.4	9.7
2.4 GeV Data Bins						
No.	Q^2	W	ϵ	p_e	θ_e	θ_γ
1	0.5	1.7	0.68	1.06	25.6	17.7
2	1.0	1.7	0.48	0.80	42.4	16.5
3	1.5	1.7	0.26	0.53	65.8	12.5
4	0.5	1.9	0.46	0.68	32.2	11.2
5	1.0	1.9	0.23	0.41	60.3	9.3
6	0.5	2.1	0.16	0.25	54.0	5.2

Table 1: Kinematic variables for our chosen bins of Q^2 and W for beam energies of 2.4 and 4.0 GeV. Energies and momenta in GeV and angles in degrees.

This expression can be used to determine the number of counts required to achieve a given statistical measurement accuracy for an assumed Λ polarization. This expression also makes it very clear that the statistical uncertainty goes as $1/\eta$, the electron beam polarization. Thus the *highest* possible beam polarization achievable by CEBAF is important to reduce our measurement uncertainties.

To achieve a ± 0.10 absolute statistical uncertainty in P_Λ per bin (where a bin is defined in terms of Q^2 , W , $\cos \theta_K$, ϕ_K) we need approximately 1500 counts per bin. This assumes a value of $P_\Lambda = 0$ for the sake of computation. As seen from Eq. 16, this assumption for P_Λ represents the *worst case* assumption. For a given number of counts per bin, the statistical uncertainty decreases as a function of

the magnitude of P_Λ . This estimation assumes 80% beam polarization.

In determining the statistical uncertainty for a one month running period at each beam energy, a beam polarization of 80% has been assumed. The 1997-1998 e1 data rates were extracted directly from existing data for each Q^2/W bin and then scaled according to the following considerations:

- 30 days at a given energy \times 24 hours/day \times 0.40 beam/CLAS efficiency = 288 hours of ‘good’ beam.
- DAQ speed improvement factor of 2.0.
- Second level trigger improvement factor of 2.0.
- CLAS luminosity limitation of $10^{34}/\text{cm}^2/\text{s}$

Let us discuss each of these important factors in turn.

1). The 40% efficiency factor comes from an analysis of the accelerator/CLAS efficiency during the polarized g1 running period in June/July 1998 [37]. This efficiency factor includes time lost for both accelerator and CLAS down time, and both accelerator Mött polarimeter runs and Hall B Møller polarimeter runs. With this 40% efficiency factor, we can then expect to acquire production data for 288 hours during a one month run period. Over the year that CLAS has been taking data as part of its physics program, this factor has steadily increased so further improvement may be expected.

2). During the first e1 run period, our data acquisition system acquired CLAS triggers at a rate of ~ 350 Hz. Due to improvements in the FASTBUS crate VME interface hardware and substantive improvements in CODA, this rate is expected to be closer to 1 kHz during 1999. We have conservatively estimated this speed improvement to be a factor of 2. This is the level of improvement seen in the August 1998 g1 running period.

3). During the end of 1998 the CLAS detector is expected to implement a second level trigger to improve electron selectivity. Of all triggers during the first e1 run period, only 16% of the 4.0 GeV triggers and 35% of the 2.4 GeV triggers actually contained a reconstructible scattered electron, even with the CLAS triggered on the logical AND of the electromagnetic calorimeters and the Čerenkov counters. The additional level of trigger logic requires that at least one charged particle traverses through a full drift chamber stack in any sector. The electron selectivity factor is expected to improve dramatically with the implementation

of the CLAS second level trigger. Again, we have conservatively estimated this trigger improvement to be a factor of 2.

4) With the improvement factors cited in 2) and 3), the limitation on data rate becomes the maximum CLAS luminosity of $10^{34}/\text{cm}^2/\text{s}$. This luminosity limit is set largely by two factors: first, the difficulty of reconstructing tracks in the drift chambers in a high-rate environment and second, the desire to keep total ionization within the drift chambers (particularly Region 1) down in order to maintain the chamber's life expectancy. Thus, the data rates presented here are scaled by a total factor of two compared to the existing e1 data.

Our expected counting statistics for 30 days each of 2.4 and 4.0 GeV are displayed for our desired Q^2 and W bins in Table 2 and Table 3 respectively. The statistical uncertainties are presented for different binning scenarios in $d\Omega_K$ with the same Q^2 and W bins. The statistical uncertainties included are for each $d\Omega_K$ bin within a given Q^2/W bin. It is clear from these tables that if we want to employ bins of $Q^2 = \pm 0.25 (\text{GeV}/c)^2$ and $W = \pm 0.1 \text{ GeV}$, inclusion of more than 4 θ_K/ϕ_K sub-bins severely limits the statistical precision of the polarization measurement. If more than 4 θ_K/ϕ_K bins are found to be important during the analysis, we will be forced to widen our Q^2 or W bins accordingly.

The selection of our exact choice of the sizes of the Q^2 and W bins is somewhat arbitrary, but is still essentially motivated by the physics of this process and the total counting statistics. Our goal is to make the W bins as narrow as possible. For the kinematics of interest in this proposal, $1.6 \leq W \leq 2.4 \text{ GeV}$, many intermediate overlapping resonances are present. In order to be sensitive to which of these resonances are important when attempting to describe the reaction mechanism, it is essential to maximize sensitivity to individual resonances whenever possible. As resonance widths are typically 200 - 300 MeV, 200 MeV slices in W are appropriate over our acceptance range. The selection of bin sizes in Q^2 of 500 MeV was designed to give us at least 2 bins at each W to allow study of the Q^2 dependence of the polarization and response functions.

2.4 GeV	Counts		
$Q^2 \downarrow \setminus W \rightarrow$	1.7	1.9	2.1
1.5	1147	-	-
1.0	5550	6105	-
0.5	9324	13394	1443
	Statistical Uncertainty–Choice A		
1.5	± 0.46	-	-
1.0	± 0.20	± 0.20	-
0.5	± 0.16	± 0.14	± 0.42
	Statistical Uncertainty–Choice B		
1.5	± 0.23	-	-
1.0	± 0.10	± 0.10	-
0.5	± 0.08	± 0.07	± 0.21
Q^2 bin = ± 0.25 (GeV/c) ² , W bin = ± 0.1 GeV $\cos \theta_p^{RF}$ bins = 1, ϕ_p^{RF} bins = 1			
Choice A: $\cos \theta_K$ bins = 4, ϕ_K bins = 4			
Choice B: $\cos \theta_K$ bins = 4, ϕ_K bins = 1			

Table 2: Expected 2.4 GeV counting statistics for a one month run at 80% electron beam polarization for a given choice of binning in Q^2 , W , and $d\Omega_K$.

4.0 GeV	Counts			
$Q^2 \downarrow \backslash W \rightarrow$	1.7	1.9	2.1	2.3
2.5	1325	1383	-	-
2.0	2103	3679	1037	-
1.5	5040	5184	2880	-
1.0	2477	2736	1843	1037
	Statistical Uncertainty–Choice A			
2.5	± 0.42	± 0.42	-	-
2.0	± 0.34	± 0.30	± 0.48	-
1.5	± 0.23	± 0.21	± 0.30	-
1.0	± 0.31	± 0.30	± 0.37	± 0.48
	Statistical Uncertainty–Choice B			
2.5	± 0.21	± 0.21	-	-
2.0	± 0.17	± 0.16	± 0.24	-
1.5	± 0.11	± 0.11	± 0.16	-
1.0	± 0.16	± 0.16	± 0.18	± 0.24
Q^2 bin = ± 0.25 (GeV/c) ² , W bin = ± 0.1 GeV				
$\cos \theta_p^{RF}$ bins = 1, ϕ_p^{RF} bins = 1				
Choice A: $\cos \theta_K$ bins = 4, ϕ_K bins = 4				
Choice B: $\cos \theta_K$ bins = 4, ϕ_K bins = 1				

Table 3: Expected 4.0 GeV counting statistics for a one month run at 80% electron beam polarization for a given choice of binning in Q^2 , W , and $d\Omega_K$.

4 Monte Carlo Study

In this section we present the results of our Monte Carlo study for this measurement. The purpose of the Monte Carlo study includes (1) to get a detailed acceptance function from the $\vec{e}p \rightarrow e'K^+\vec{\Lambda}$ reaction with high field e1 data using an unpolarized electron beam, and (2) to provide a good model to measure the induced/transferred polarization using a polarized electron beam. For this analysis, we wrote a code, KLAMGEN, to generate the appropriate events. This code included the electron beam helicity state and Λ polarization for each event, and used GSIM and RECSIS for simulation of the CLAS spectrometer and event reconstruction, respectively. Currently, only the 4.0 GeV results have been simulated.

In the rest of this section we will use the $(\hat{t}, \hat{n}, \hat{l})$ coordinate system as defined in Fig. 3 for the Λ polarization. As before, each polarization component (P_i , $i = t, n, l$) can be written in the form $P_i = P_i^0 + hP_i'$, where h is the beam electron helicity, P_i^0 is the induced polarization (helicity independent), and P_i' is the transferred polarization (helicity dependent). We will describe how we extract the induced polarization from the e1 data and demonstrate how we will extract the induced/transferred polarization utilizing two electron helicity states by our Monte Carlo study.

4.1 Generation of $\vec{e}p \rightarrow e'K^+\vec{\Lambda}$

After selecting the beam energy, 5 quantities are necessary to completely characterize the $\vec{e}p \rightarrow e'K^+\vec{\Lambda}$ reaction in the laboratory system.

- Scattered electron: the momentum and angles (p_e, θ_e, ϕ_e) of the scattered electron are randomly generated in such a way that W and ϕ_e have a uniform distribution in phase space, and Q^2 has a $1/Q^4$ dependence in phase space to maximize the efficiency as shown in Figs. 19a and 19b.
- Electroproduced kaon: the angles (θ_K, ϕ_K) of the electroproduced kaon are generated isotropically as shown in Figs. 19c and 19d.

In addition to these quantities, the reaction (x, y, z) position is also generated at the target. Currently, we are assuming a point target.

The events from KLAMGEN are thrown into GSIM, which uses the GEANT routines from the CERN libraries as a framework for a Monte Carlo simulation of the CLAS detector. Momentum, angles, and position of each particle at the target are reconstructed using RECSIS, the standard CLAS analysis software package.

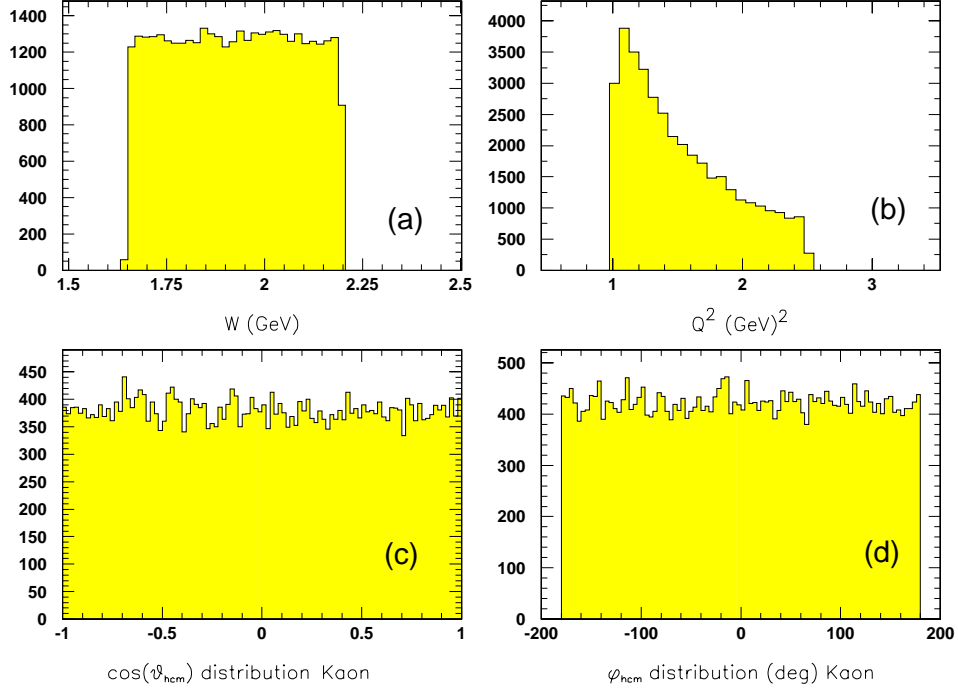


Figure 19: Event distributions generated by KLAMGEN for 4.0 GeV incident electrons. (a) W (GeV), (b) Q^2 (GeV/c)², (c) $\cos \theta_K$, and (d) ϕ_K (deg).

This simulation includes, therefore, the effects of (1) the geometrical acceptance, (2) the electroproduced kaon decay probability, and (3) the particle identification efficiency based on the time of flight information. The event reconstruction is shown in Fig. 20 for $W = 1.6 - 2.2$ GeV and $Q^2 = 1.0 - 2.5$ (GeV/c)². Fig. 20a shows the reconstructed Λ missing mass spectrum with a requirement of good (decay) π^- missing-mass reconstruction as shown in Fig. 20b. Figs. 20c and 20d show the reconstructed $\cos \theta_K$ and ϕ_K distributions of the kaon in the center-of-momentum frame. The width of the Λ missing-mass peak is 9.6 MeV from Monte Carlo, and is 11.2 MeV from the 4.0 GeV e1 data as shown in Fig. 18. The difference between the Monte Carlo and the e1 data can be explained by the following:

- A perfect resolution of the drift chambers is assumed in our simulation of GSIM.

- Radiative effects are not considered.
- A point energy resolution of the incident electron is assumed.
- A point position resolution of the target is assumed.

The above features will be implemented in our Monte Carlo in the near future.

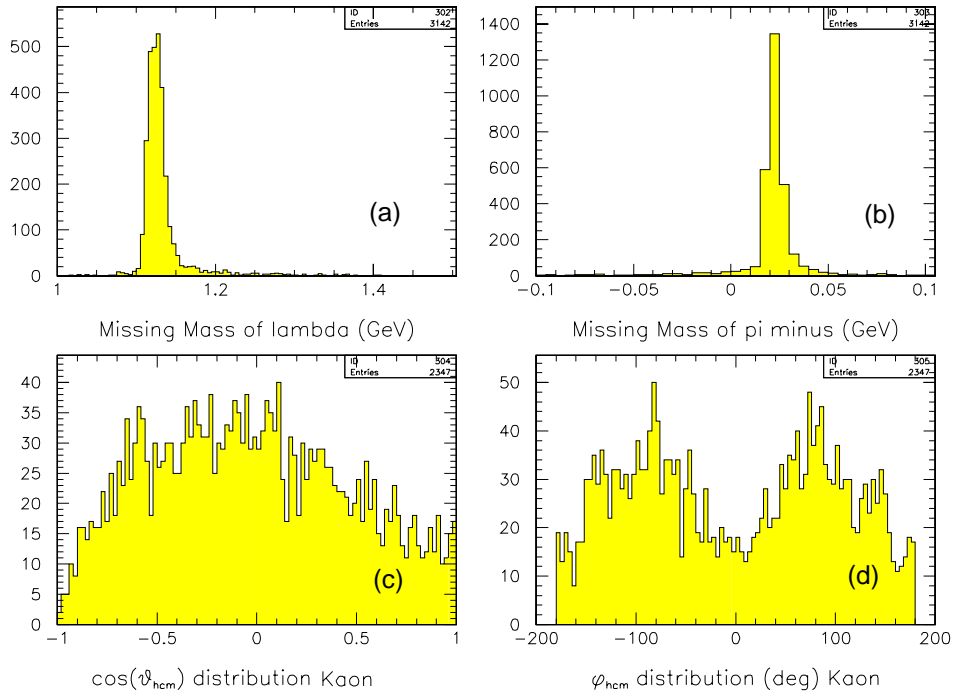


Figure 20: Monte Carlo event reconstructions for 4.0 GeV incident electrons with 90% torus field. (a) Missing mass of Λ (GeV), (b) Missing mass of π^- (GeV), (c) $\cos \theta_K$, and (d) ϕ_K (deg).

4.2 Generation of $\Lambda \rightarrow p + \pi^-$

Momentum and angles of the Λ decay protons from $\Lambda \rightarrow p + \pi^-$ are generated isotropically in the Λ rest frame. From conservation of energy and momentum in

the Λ rest frame—which will be hereafter referred to as the RF system—the proton energy and momentum are first calculated:

$$E_p^{RF} = \frac{M_\Lambda^2 + M_p^2 - M_\pi^2}{2M_\Lambda}, \quad p_p^{RF} = ((E_p^{RF})^2 - (M_p)^2)^{1/2} \quad (17)$$

We then apply the general Lorentz transformation to calculate the momentum and the energy of the proton in the laboratory system. The entire reaction is identified by the pion missing mass spectrum as shown in Fig. 20b. The main purpose of this study is to evaluate the acceptance function of $\cos \theta_p^{RF}$ for all three n , l , and t directions. The first row of Fig. 21 shows the $\cos \theta_p^{RF}$ distributions from KLAMGEN and the second row of Fig. 21 shows the $\cos \theta_p^{RF}$ distributions from event reconstruction after GSIM and RECSIS. The third row of Fig. 21 shows the acceptance-correction function for each component, which is the ratio of the second to first rows. Columns 1,2, and 3 correspond to the \hat{l} , \hat{t} , and \hat{n} components respectively.

4.3 Measurement of Induced Polarization of Λ

Once the scattered electron, kaon, and Λ -decay proton are detected, the entire reaction is identified by the Λ and π^- missing mass cuts. Since no polarized electron beam was used during the first 4.0 GeV e1 run, we can only measure the *induced* Λ polarization. The measured angular distributions of protons are affected by the CLAS acceptance, and this is corrected by the acceptance function obtained in the previous section. Fig. 22 shows the angular distribution of the protons in the RF system. Again, columns 1,2, and 3 correspond to the \hat{l} , \hat{t} , and \hat{n} components respectively. The first row is for the e1 data, the second row is the acceptance-correction functions obtained in the previous section, and the last row is the acceptance corrected angular distributions. From this, the Λ polarization can be determined by performing a linear parameterization of the polar angular distribution of the proton:

$$N(\theta_p^{RF}) = B + A \cos(\theta_p^{RF}), \quad A = \frac{\alpha P_\Lambda}{2}, \quad B = \frac{1}{2} \quad (18)$$

Table 4 shows the measured induced polarization of the Λ for the e1 run in March 1998. We analyzed 70% of the e1 data at 4.0 GeV with 90% torus field. The data is accumulated in a single Q^2 and W bin. Systematic uncertainties were estimated by a) analyzing simulated data and b) studying the dependence of the variations of applied cuts on the missing mass spectra of the Λ and π^- . A detailed discussion of systematic uncertainties is included in Sec. 5. Both P_l and

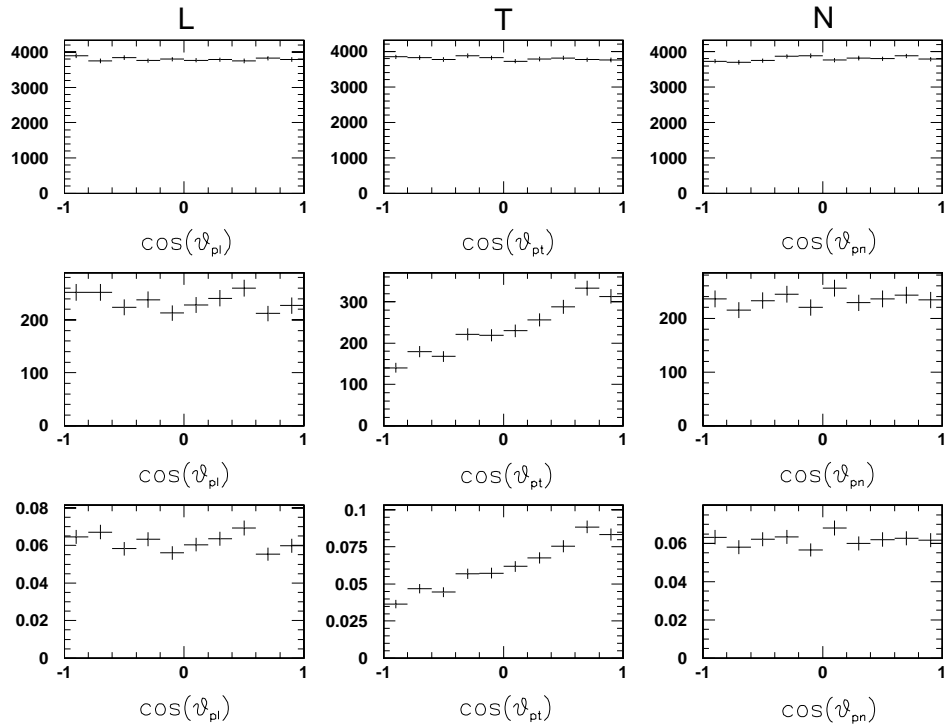


Figure 21: The first row is the proton angular distributions generated at 4.0 GeV with KLAMGEN, the second row is from the Monte Carlo event reconstruction, and the third row is the acceptance-correction function. The first column is for \hat{l} , the second is for \hat{t} , and the third is for \hat{n} .

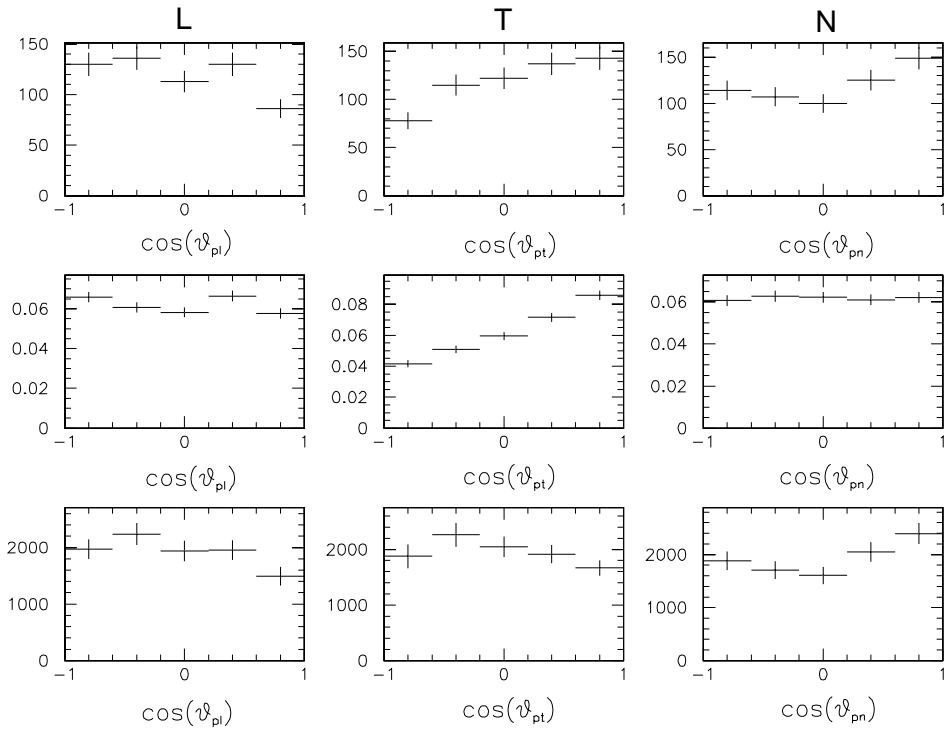


Figure 22: The first row is the reconstructed decay-proton angular distributions from the 4.0 GeV e1 data, the second row is the Monte Carlo CLAS acceptance-correction function (rebinned to match the data), and the third row is the acceptance corrected e1 data. The first column is for \hat{l} , the second is for \hat{t} , and the third is for \hat{n} .

P_t are expected to be zero due to parity considerations, however, a more thorough study of acceptance corrections and Σ^0 background remains to be completed. P_n has not been shown since it is not known what its value should be for the W - and Q^2 -integrated data.

-	polarization	statistical uncertainty	estimated systematic uncertainty
P_l	0.132	0.086	0.058
P_t	0.129	0.075	0.054

Table 4: Polarization P_l and P_t for the 4.0 GeV e1 data from March 1998 with 90% torus field.

4.4 Simulation of the Transferred/Induced Λ Polarization

Since there were no data acquired with a polarized electron beam during the first e1 run period, we will rely on our Monte Carlo study to evaluate transferred/induced polarization measurements of the Λ . To make our simulation more realistic, we use the following approach:

- One of the electron helicity states (+ or $-$) is randomly generated for each event.
- Six asymmetries are given for transferred/induced polarization (P_i^+ and P_i^- , $i = n, l, t$). We choose 30% for P_i^+ and -10% for P_i^- as shown in Fig. 23. In Fig. 23, columns 1,2, and 3 correspond to \hat{l} , \hat{t} , and \hat{n} components respectively. The first row is from the sum of the helicity (+) and helicity ($-$) states, the second row is from the helicity (+) state, and the third row is from the helicity ($-$) state. These asymmetries contain the contribution from all the polarization dependent response functions.

These events are thrown into GSIM and are reconstructed using RECSIS as shown in Fig. 24. The description of Fig. 24 is the same as Fig. 23. We can reconstruct the six transferred/induced polarization components in two ways.

1. The reconstructed angular distribution is corrected by the CLAS acceptance, and the polarization for each electron helicity state is measured.

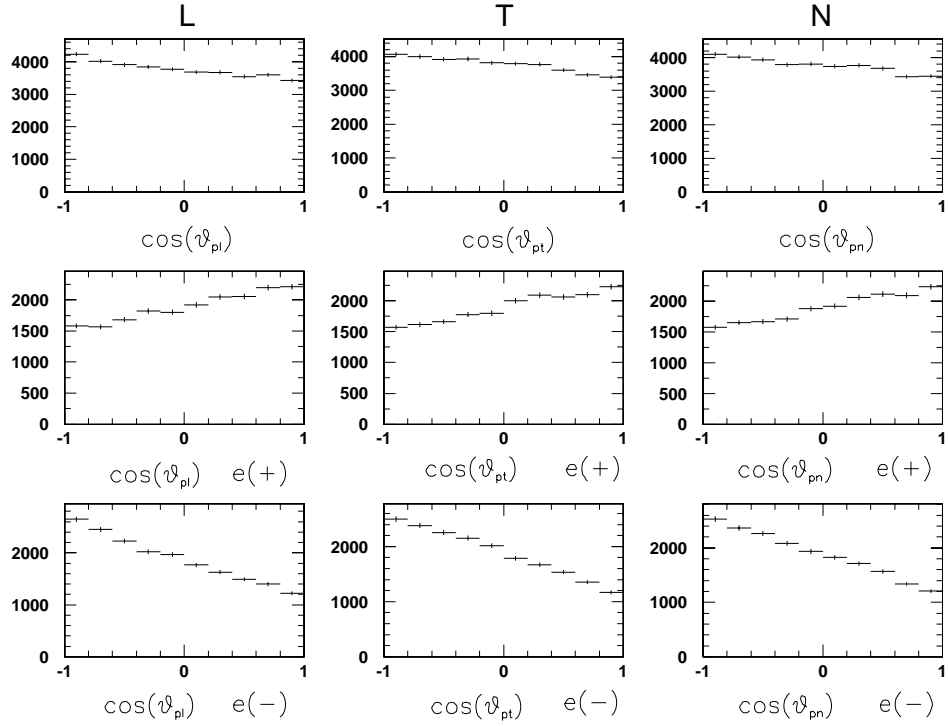


Figure 23: Proton angular distributions generated by KLAMGEN that include the electron helicity states and the polarized Λ . The first row is from the sum of the two electron helicity states, the second is for the (+) electron helicity state, and the third is for the (-) electron helicity state. The first column is for \hat{l} , the second is for \hat{t} , and the third is for \hat{n} . 30% polarization and -10% polarization are chosen for P_i^+ and P_i^0 , respectively for each of the three components. So the Λ polarization is 20% for the (+) electron helicity state and -40% for the (-) electron helicity state, and -20% for the sum of the two electron helicity states

2. Without including acceptance corrections, take a ratio of the reconstructed angular distributions from each electron helicity state and extract the polarization. This ratio can then be fit to the following function:

$$\frac{N^+}{N^-} = C \frac{1 + \alpha P^+ \cos \theta_p^{RF}}{1 + \alpha P^- \cos \theta_p^{RF}} \quad (19)$$

where C is a constant. The ratio will be independent of any acceptance corrections if the corrections for N^+ and N^- are the same. Once the polarization of each electron helicity state is measured, the transferred/induced polarization can be determined:

$$P_i^0 = \frac{P_i^+ + P_i^-}{2}, \quad P_i' = \frac{P_i^+ - P_i^-}{2}, \quad i = n, l, t \quad (20)$$

We analyzed P_n from simulated data using both methods described above. The result using the first method is shown in Fig. 25 and Table 5. The top (bottom) of Fig. 25 shows the angular distribution of the protons along the \hat{n} direction in the RF system from the $+$ ($-$) electron helicity state after it has been acceptance corrected.

The results using the second method are shown in Fig. 26 and Table 5. Fig. 26 (a) shows the angular distribution of the proton from the $(+)$ electron helicity state and Fig. 26 (b) from the $(-)$ electron helicity state. Fig. 26 (c) shows the ratio (N^+/N^-) of the two electron helicity states.

Method	P_n^+	P_n^-	P_n^0	P_n'
# 1	0.195 ± 0.032	-0.386 ± 0.043	-0.096 ± 0.054	0.295 ± 0.054
# 2	0.180 ± 0.021	-0.401 ± 0.028	-0.111 ± 0.035	0.290 ± 0.035

Table 5: Polarization P_n from simulated data using the methods described in the text. Uncertainties are combined statistical and acceptance correction uncertainties for the 40000 events used in the Monte Carlo .

We note that the initial P_n^0 and P_n' were -0.10 and 0.30 , respectively. As shown in the Table 5, the second method has a substantial advantage since there is no acceptance involved in the measurement assuming that the acceptance of the $(+)$ electron helicity state is equal to that of the $(-)$ electron helicity state. Comparison of the results for the two methods for large helicity dependent polarizations, P' , should provide a cross check on our acceptance corrections. One

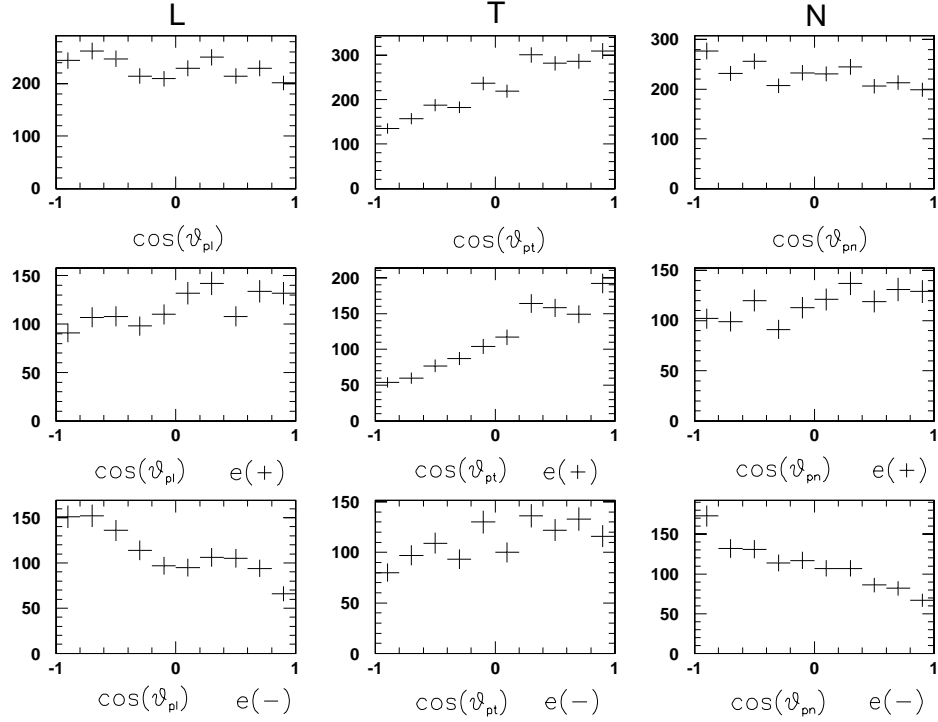


Figure 24: Reconstructed proton angular distributions from Monte Carlo simulations. The first row is from the sum of the two electron helicity states, the second is for the (+) electron helicity state, and third is for the (-) electron helicity state. The first column is for \hat{l} , the second is for \hat{t} , and the third is for \hat{n} .

disadvantage of the second method is that if the helicity dependent polarization is zero or small, this method becomes impossible or very difficult since the ratio in Eq. 19 approaches a constant.

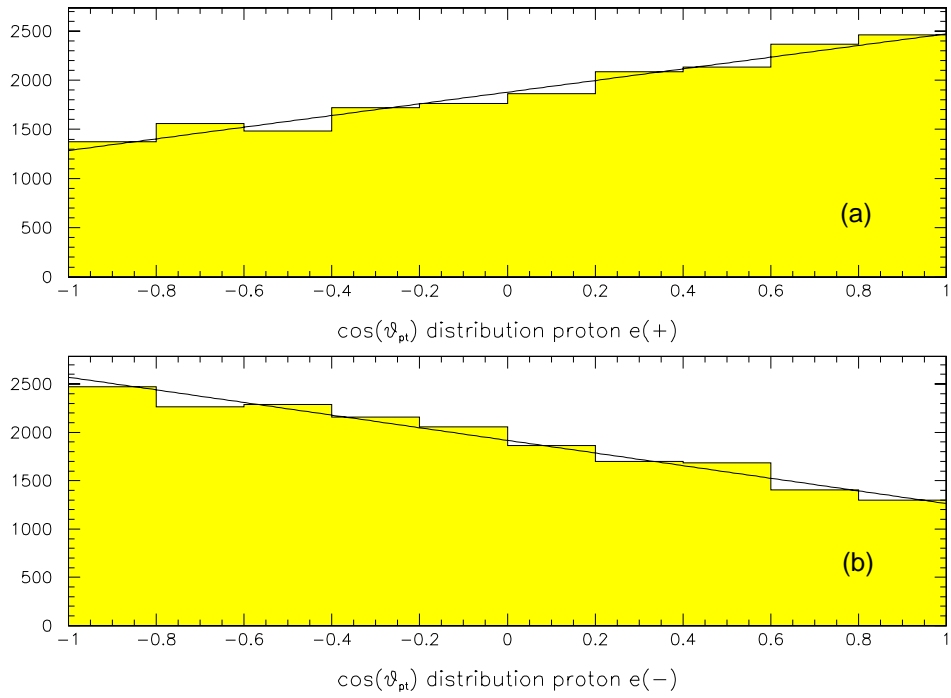


Figure 25: Monte Carlo for: (a) acceptance corrected proton angular distribution for the \hat{n} direction from the (+) electron helicity state. (b) acceptance corrected proton angular distribution for the \hat{n} direction from the (-) electron helicity state.

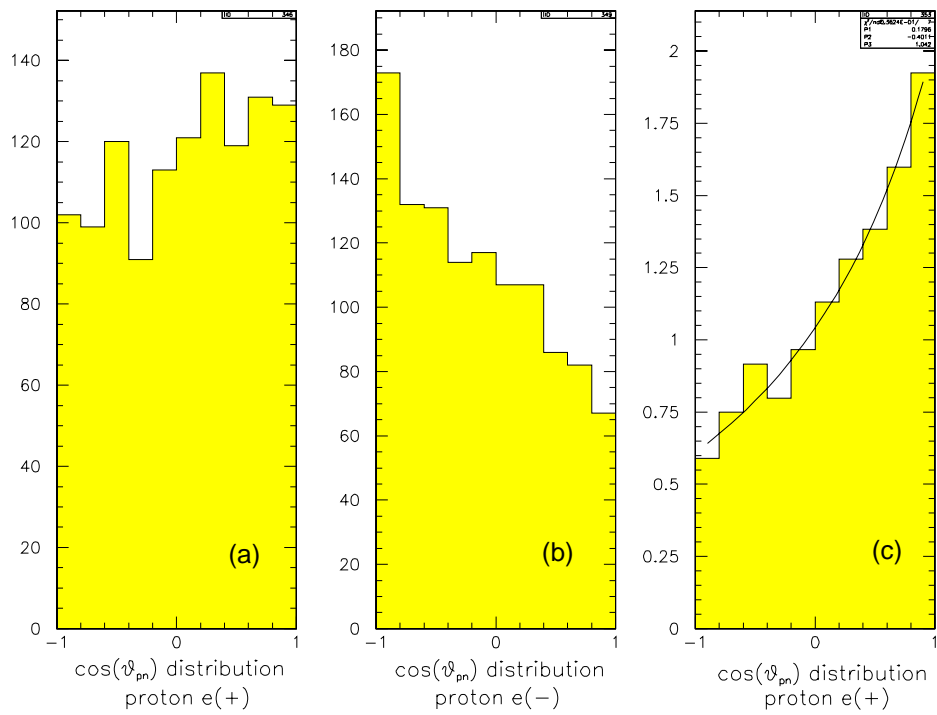


Figure 26: Monte Carlo for: (a) The proton angular distribution for the \hat{n} direction from the (+) electron helicity state. (b) The proton angular distribution for the \hat{n} direction from the (-) electron helicity state. (c) The ratio of the angular distributions from the two electron helicity states.

5 Systematic Uncertainties

There are two primary sources of systematic uncertainties: uncertainties associated with determination of the kinematic variables (Q^2 , W , $\cos(\theta_K)$, ϕ_K , etc.), and uncertainties associated with conditions of the experimental apparatus. The effects of these are also somewhat different for each polarization component. Since we measure each polarization component integrated over ϕ_K , there is no helicity dependent component in P_n (P_y). This means that we need to know the CLAS acceptance of the decay protons well since we cannot use the ratio method (#2) described previously. On other hand, there is no helicity independent polarization component for P_t and P_l , but we have an uncertainty due to the electron beam polarization.

Table 6 summarizes the sources and estimated individual systematic uncertainties. The total is the sum of all individual sources of uncertainties in quadrature. All estimates are preliminary and we are continuing our Monte Carlo study to improve our understanding of the systematics.

Source of uncertainty	σ_{P_n}	σ_{P_l}	σ_{P_t}
Beam helicity	0.0	0.030	0.030
Proton Acceptance	0.040	0.00	0.00
Background (Σ^0 , π^+ etc.)	0.030	0.030	0.030
Angle	0.015	0.015	0.015
Momentum	0.025	0.025	0.025
Beam energy	0.010	0.010	0.010
Radiative Corrections	0.015	0.015	0.015
total	0.061	0.055	0.055

Table 6: A list of various sources of systematic uncertainties for each polarization component at 4.0 GeV. Comparable uncertainties are expected at 2.4 GeV.

In the end we will also have a number of self-consistency checks which will help us better understand our systematic uncertainties. As pointed out in Sec. 2.1, \mathcal{P}_x^0 , \mathcal{P}_y^0 , and \mathcal{P}_z^0 should all be zero. Deviations from zero will indicate problems with acceptance or energy calibrations. We can also bin data on a CLAS sector-by-sector basis so that any sector dependencies can be determined and corrected.

Included in our table of systematic errors is an entry for background contamination. As mentioned earlier, our Λ missing mass spectrum is contaminated mainly by the $ep \rightarrow e'\pi^+\Delta^0$ reaction, where the pions are misidentified as kaons.

This contribution is effectively removed with a cut on the π^- missing mass in the $p(e, e'K^+p)$ reconstruction. The other important background reaction to consider is $ep \rightarrow e'K^+\Sigma^0$, where the Σ^0 polarization contaminates the Λ polarization. As stated earlier, our cut on Λ missing mass will include a $\sim 15\%$ contamination from Σ^0 s due to the resolution of CLAS that must be taken into account. Presently no electroproduction data exist for either the induced or transferred Σ^0 polarization. However, these quantities for the Σ^0 have been calculated for photoproduction [2]. These calculations show that the Σ^0 polarization has comparable magnitude to the predicted Λ polarization, but is typically opposite in sign. Our best recourse in attempting to understand the data is to measure the Σ^0 polarization components and then account for their affect on the Λ polarization.

6 Summary

This proposal describes a new experiment to study polarization observables in strangeness electroproduction at 2.4 and 4.0 GeV using the $\vec{e}p \rightarrow e' K^+ \vec{\Lambda}$ reaction. The large acceptance of CLAS will allow us to efficiently detect the scattered electron, kaon, and the decay proton from the Λ over a range of Q^2 from 0.4 to 2.7 (GeV/c)² and W from 1.6 to 2.4 GeV. Measurement of the angular correlation of the decay proton will allow a determination of the Λ polarization. Due to the large phase space coverage of CLAS, this experiment provides a unique opportunity to probe the response functions for this process beyond the usual choices of parallel or in-plane kinematics. Our proposal seeks to measure the six electron beam helicity-dependent and helicity-independent polarization components of the Λ . Some of these polarization components show strong model sensitivity as well as sensitivity to Λ magnetic form factor and the $K^+ K^{*+} \gamma$ transition form factor. We conclude this summary section with the following remarks:

- The CLAS detector has a sizeable three-body final-state acceptance for the scattered electron, electroproduced kaon, and the decay proton from the reconstructed Λ hyperon that enable the first serious attempt at measuring the double-polarization observables in this energy regime over a broad range of Q^2 , W , t , and ϕ_K . While E98-101 in Hall C claims better statistical precision over a limited kinematical region, this will extend the measurements to kinematics simply not accessible with other detector systems. In all, we expect to get data at 18 different kinematical settings (E , Q^2 , and W) each with four points in θ_K and each point allowing extraction of all three components of the recoil polarization.
- The CLAS spectrometer has a large and uniform acceptance in $\cos \theta_K$ and ϕ_K which allows for a reliable determination of the t dependence of the response functions $R_{TT'}$ and $R_{TL'}$.
- We have attempted to stress the importance of performing this experiment with the highest possible electron beam polarization available for the accelerator to achieve the smallest possible statistical uncertainties on these measurements.
- Our detailed analysis of the existing unpolarized 2.4 and 4.0 GeV data has enabled us to provide an accurate—and realistic—determination of our expected statistical uncertainties. We have shown that a one month run

at each beam energy and 80% beam polarization will enable us to measure the Λ polarization components with an average statistical accuracy of approximately ± 0.10 for 2.4 GeV and ± 0.14 for 4.0 GeV .

- We have made initial attempts to study the level of systematic errors with real data. Preliminary results indicate that these seem to be well less than 10%.
- The data are expected to provide for a unique opportunity for the further development of hadrodynamical models, quark-based models, and models based on Regge exchanges. It is expected that detailed comparisons of these models to the observables of electroproduction, beyond allowing for improvements to these theories, will help to quantify the transition from the non-perturbative to perturbative QCD.
- This collaboration looks forward as well to extending this work to the 6.0 GeV regime over the next few years to pursue this physics beyond the resonance region.

7 Beam-time Request

To have a significant physics impact, this experiment requires a minimum of 30 days of 80% polarized electron beam at 4.0 GeV. In principle, our proposal requires no new beam time. The experiment uses the standard Hall B liquid hydrogen target with the CLAS spectrometer at maximum field for the 4.0 GeV running. This is compatible with current e1 run period plans. Our trigger requirements—requiring the highest efficiency electron trigger—are also compatible with the experiments of the e1 run-period. The only difference is that we request high-polarization beam. The current Jefferson Lab run schedule includes 11 days each of high polarization 4.0 and 4.4 GeV running and 10 days of 4.2 GeV running in early 1999.

The schedule also includes 12 days of 2.6 GeV running in the same period. Taking this data with high polarization beam would result in statistical uncertainties about 1.6 times larger than quoted in Table 2 but would still make notable improvements to kaon-electroproduction data base. Significant improvements to the statistical accuracy of our data would be made if the entire remaining e1 running (approximately four months) is done at 2.4 and 4.0 GeV (the latter is preferable) with the highest possible beam polarization.

8 Appendix

8.1 Kinematics

Here we define the kinematical variables used throughout the text.

The virtual photon flux is

$$\Gamma = \frac{\alpha}{4\pi^2} \frac{kE'}{Q^2 E} \left(\frac{2}{1-\epsilon} \right)$$

where E and E' incident and scattered electron energies respectively,

$$k = \frac{W^2 - M^2}{2M},$$

the invariant mass of the hadronic state is

$$W^2 = M^2 + 2M\nu - Q^2,$$

the four-momentum transfer squared is

$$Q^2 = -q^2 = 4EE' \sin^2 \theta / 2,$$

and the energy transfer is

$$\nu = E - E'.$$

The transverse polarization of the virtual photon is

$$\epsilon = \left(1 + 2 \left(1 + \frac{\nu^2}{Q^2} \right) \tan^2 \frac{\theta_{E'}}{2} \right)^{-1}$$

and the longitudinal polarization of the virtual photon is

$$\epsilon_L = \frac{Q^2}{\nu^2} \epsilon.$$

We have defined

$$K = \frac{|\mathbf{k}|}{k_\gamma^{cm}}$$

where k_γ^{cm} is the virtual photon momentum in the c.m. system, $|\mathbf{k}|$ is the c.m. momentum of the kaon.

8.2 Response functions

β	α	T	L	^cTL	^sTL	^cTT	^sTT	$^c\text{TL}'$	$^s\text{TL}'$	TT'
-	-	R_T^{00}	R_L^{00}	R_{TL}^{00}	0	R_{TT}^{00}	0	0	$R_{TL'}^{00}$	0
-	x	0	0	0	R_{TL}^{0x}	0	R_{TT}^{0x}	$R_{TL'}^{0x}$	0	$R_{TT'}^{0x}$
-	y	R_T^{0y}	R_L^{0y}	R_{TL}^{0y}	0	‡	0	0	$R_{TL'}^{0y}$	0
-	z	0	0	0	R_{TL}^{0z}	0	R_{TT}^{0z}	$R_{TL'}^{0z}$	0	$R_{TT'}^{0z}$
x'	-	0	0	0	$R_{TL}^{x'0}$	0	$R_{TT}^{x'0}$	$R_{TL'}^{x'0}$	0	$R_{TT'}^{x'0}$
y'	-	$R_T^{y'0}$	‡	‡	0	‡	0	0	‡	0
z'	-	0	0	0	$R_{TL}^{z'0}$	0	$R_{TT}^{z'0}$	$R_{TL'}^{z'0}$	0	$R_{TT'}^{z'0}$
x'	x	$R_T^{x'x}$	$R_L^{x'x}$	$R_{TL}^{x'x}$	0	‡	0	0	$R_{TL'}^{x'x}$	0
x'	y	0	0	0	‡	0	‡	‡	0	‡
x'	z	$R_T^{x'z}$	$R_L^{x'z}$	‡	0	‡	0	0	‡	0
y'	x	0	0	0	‡	0	‡	‡	0	‡
y'	y	‡	‡	‡	0	‡	0	0	‡	0
y'	z	0	0	0	‡	0	‡	‡	0	‡
z'	x	$R_T^{z'x}$	‡	$R_{TL}^{z'x}$	0	‡	0	0	$R_{TL'}^{z'x}$	0
z'	y	0	0	0	‡	0	‡	‡	0	‡
z'	z	$R_T^{z'z}$	‡	‡	0	‡	0	0	‡	0

Table 7: Response functions for pseudoscalar meson production [16]. The target (recoil) polarization is indicated by α (β). The last three columns are for when the electron is polarized. ‡ indicates a response function which does not vanish but is related to other response functions.

References

- [1] R. A. Adelseck and B. Saghai, Phys. Rev. **C42**, 108 (1990).
- [2] J. C. David, C. Fayard, G. H. Lamot, and B. Saghai, Phys. Rev. **C53**, 2613 (1996); T. Mizutani, C. Fayard, G.-H. Lamot, B. Saghai, Phys. Rev. **C58**, 75 (1998).
- [3] Robert A. Williams, Chueng-Ryong Ji, and Stephen R. Cotanch, Phys. Rev. **C46**, 1617 (1992).
- [4] S. Capstick and W. Roberts, Pre-print nucl-th/9804070, (1998).
- [5] M. Vanderhaeghen, et al., Phys. Rev. **C57**, 1454, (1998).
- [6] O. K. Baker *et al.*, CEBAF Proposal E93-018.
- [7] B. Zeidman *et al.*, CEBAF Proposal E91-016.
- [8] G. Niculescu *et al.*, Phys. Rev. Lett. **81**, 1805 (1998).
- [9] P. Markowitz *et al.*, CEBAF Proposal E94-108.
- [10] K. H. Hicks *et al.*, CEBAF Proposal E93-030.
- [11] R. A. Schumacher *et al.*, CEBAF Proposal E89-004.
- [12] L. Dennis *et al.*, CEBAF Proposal E89-043.
- [13] O. K. Baker *et al.*, JLab Proposal E98-101.
- [14] A.Bravar *et al.* Preprint FermiLab-Pub-96/393-E E704 (1997).
- [15] M. Guidal, et al., Nucl. Phys. **A627**, 645, (1997).
- [16] G. Knöchlein, D. Drechsel, L. Tiator, Z. Phys. **A 352**, 327 (1995).
- [17] C. N. Brown *et al.*, Phys. Rev. Lett. **28**, 1086 (1972); T. Axemoon *et al.*, Nucl. Phys. **B95**, 77 (1975); C. J. Bebek *et al.*, Phys. Rev. D **15**, 594 (1977); **15**, 3082 (1977); P. Brauel *et al.*, Z. Phys. **C3**, 101 (1979).
- [18] C. J. Bebek *et al.*, Phys. Rev. D **17**, 1693 (1978).
- [19] B. Borgia *et al.*, Nuovo Cimento **32**, 218 (1964); M. Grilli *et al.*, *ibid.* **38**, 1467 (1965); D. E. Groom and J. H. Marshall, Phys. Rev. **159**, 1213 (1967); R. Hass *et al.*, Nucl. Phys. **B137**, 261 (1978).

- [20] K. H. Althoff *et al.*, Nucl. Phys. **B137**, 269 (1978).
- [21] T. Mart, private communication, (1998).
- [22] R. A. Adelseck and L. E. Wright, Phys. Rev. C **38**, 1965 (1988); R. Adelseck, Ph.D. thesis, Ohio University, 1988.
- [23] C. Bennhold, Phys. Rev. **C43**, 775 (1991)
- [24] T. Feuster and U. Mosel, Pre-print nucl-th/9803057, (1998).
- [25] H. Haberzettl, C. Bennhold, T. Mart, T. Feuster, Phys. Rev. **C58**, R40, (1998).
- [26] L. Micu, Nucl. Phys. **B10**, 521, (1969).
- [27] A. LeYaouanc *et al.*, Phys. Rev **D8**, 2223, (1973); Phys. Rev. **D9**, 1415, (1974); Phys. Rev. **D11**, 1272, (1975).
- [28] E.S. Ackleh, Phys. Rev. **D54**, 6811, (1996).
- [29] J.W. Alcock *et al.*, Z. Phys. **C25**, 161, (1984); S. Kumano and V.R. Pandharipande, Phys. Rev. **D38**, 146, (1988).
- [30] T. Barnes, private communication, (1998).
- [31] S. Capstick, private communication, (1998).
- [32] F. Gutbrod and G. Kramer, Nucl. Phys. **B49**, 461, (1972).
- [33] F.A. Berends, Phys. Rev. **D1**, 2590, (1972).
- [34] N. Levy *et al*, Nucl. Phys. **55**, 493, (1973).
- [35] J.M. Laget, private communication, (1998).
- [36] Calculations by J.M. Laget, unpublished, (1998).
- [37] R.A. Schumacher, g1 Experiment Coordinator, private communication, 1998.
- [38] M.D. Mestayer, private communication, (1998).
- [39] M.I. Adamovich *et al.*, Z. Phys. **A350**, 379, (1995).